Structure and texture simulations in fusion welding processes – comparison with experimental data

Chengdan Xue, Nicolas Blanc, Fabien Soulié, Cyril Bordreuil, Frédéric Deschaux-Beaume, Gildas Guillemot, Michel Bellet, Charles-André Gandin

HAL Id: hal-03519180
https://hal.science/hal-03519180

Submitted on 10 Oct 2022

Structure and texture simulations in fusion welding processes – comparison with experimental data

Chengdan Xue [a], Nicolas Blanc [b], Fabien Soulié [b], Cyril Bordreuil [b], Frédéric Deschaux-Beaume [b], Gildas Guillemot [a], Michel Bellet [a], Charles-André Gandin [a,*]

[a] *MINES ParisTech, PSL Research University, Centre de Mise en Forme des Matériaux, CNRS UMR 7635, CS 10207, 1 rue Claude Daunesse, 06904 Sophia Antipolis, France*
[b] *LMGC, Univ. Montpellier, CNRS, Montpellier, France*

The Cellular Automaton-Finite Element (CAFE) method is used to simulate grain structure evolution during gas tungsten arc welding of 316 L steel plates. The experimental configuration is designed for in-situ observations of the melt pool and liquid flow. It is complemented by electron back scattered diffraction analyses to reveal the texture resulting from melting and solidification. Simple configurations are used to facilitate comparisons with simulations, that consider no addition of metal (remelting process) and constant power for two welding speeds. It is found that the melt pool shape can be very well retrieved for the two welding speeds providing that the relation between the dendrite tip growth velocity and the undercooling is adjusted. As a result, the computed grain structure reaches good agreement with measurements in terms of morphology, orientation and texture. A standard growth kinetics model underestimates the melt pool shape and results in large deviation of the simulated grain structure with measurements. The plate subsidence after processing reaches a maximum deflection at the center of the weld seam. It is also measured and compared to the simulations that include free metal/gas boundaries, showing satisfying results despite a weaker calculated fluid flow. Finally, the chaining and coupling schemes of the CAFE model are both studied in order to quantitatively evaluate their roles on the predicted melt pool shape and grain structure. The coupling scheme reveals better coherency between macroscopic results and grain structure simulation.

1. Introduction

Fusion welding processes applied to metallic alloys aim at joining pieces of dissimilar types, natures, or properties to develop an assembled part with enhanced functionalities, also ensuring material continuity. These processes have been largely improved by industries to propose joining solutions for high thickness pieces, complex geometries, or innovative alloys [1]. However, during the solidification stage, several types of defects may develop such as porosity, crack, or segregation [2]. These defects decrease the end-use properties and quality of the welded parts also considering the loss of time and the cost required for their detections and the necessary repair work in an industrial context. Likewise, the use of improved heat sources increasing productivity is also limited by these defects. Among the latter, hot cracking is one of the most observed defects in fusion welding processes. It occurs inside the solidifying mushy region where solid is sufficiently developed to build up stresses causing a crack that cannot be healed by

the flow of liquid metal [2]. Hot cracking prevents the use of materials with a large solidification interval [3] as well as the use of more efficient process conditions leading to stress increase [4]. But it is also influenced by the morphology of the grain structure: a fine microstructure decreases the sensitivity to hot cracking by local redistribution of the deformation, the slips at grain boundaries being better absorbed [5]. Similarly, the disorientation angle at grain boundaries also influences hot cracking sensitivity [2, 6]. It is worth noticing that ultrasonic Non-Destructive Testing (NDT) is currently used to detect, localize, and estimate welding defects [7] with large dependence of ultrasound propagation to the microstructure [8]. Thus, the development of a reliable model to predict grain structure formed in fusion welding processes aims at improving our understanding for the occurrence of defects during solidification as well as the performances of NDT software that could then rely on the spatial distribution of crystal orientations in three dimensions, hence proposing a more efficient solution to defect detection.

---

* Corresponding author.
  E-mail address: Charles-Andre.Gandin@minesparis.psl.eu (C.-A. Gandin).

The CAFE model couples the Cellular Automaton (CA) method with the Finite Element (FE) method to predict the development of dendritic grain structures in solidification processing [9,10]. While applications were initially dedicated to investment casting [11–13], first examples for welding and continuous casting were very soon demonstrated [11,13]. Chen et al. [14,15] added coupling with a level set (LS) formulation to follow the evolving metal/gas boundary during Gas Metal Arc Welding (GMAW) while computing the as-built grain structure resulting from several passes to fill in a chamfer. Similar welding simulations were proposed, using more or less sophisticated description of heat and mass transfer [16–19]. However, only comparisons of the grain morphology with experimental observations were illustrated and little validation with texture formation, melt pool shape and temperature and fluid velocity fields were conducted.

The CA methodology is nowadays increasingly used for additive manufacturing processes [20–24]. More efforts are being made for comparison with Electron Back Scattered Diffraction (EBSD) maps that reveal the texture resulting from the layer-by-layer construction of parts for various scanning strategies of the heat source. A simple chaining is then used, with the computed temperature field serving as an input to the prediction of the grain structure by the CA method. While this is certainly the simplest way to link grain structure to heat flow, no study is available to evaluate the effect of this approximation. Indeed, the heat flow itself is the result of an estimated solidification path that depends on the development of the grain structure. This coupling scheme has neither been accounted for in the context of welding processes nor for additive manufacturing processes.

The confrontation of CA grain structures with measurements were conducted based on average behaviors, typically considering average grain size and texture [25]. Recently, more in-depth studies have been carried out by considering large Phase Field (PF) simulations of directionally solidified dendritic microstructures for given bi-crystal configurations, temperature gradient and isotherm velocity. Although only two-dimensional, these PF simulations required a massively parallel computational architecture using graphics processing units. The orientation of the grain boundary (GB) could then be compared with CA predictions [26,27]. Results show that the CA algorithm is capable of predicting a meaningful grain orientation in most situation considering an adjustment of the cell size with some dendritic length scales characterized at the grain boundary. For a convergent GB, i.e. when the closest primary dendrites of the two grains forming the GB converge towards each other, the GB orientation is simply given by the orientation of the best aligned primary dendrite. This is well retrieved by CA simulations considering a cell size of the order or greater than the distance between the stationary primary dendrite tips of the two grains at the GB [26]. For a diverging GB, when the closest primary dendrites forming the GB diverge, the liquid region at the GB is filled by secondary and tertiary branches. It was found that the active secondary dendrite arm spacing at the time of creation of the new tertiary dendrite arm that will finally become a stable primary dendrite is the relevant length scale to use in CA simulations [10,27]. The latter active secondary dendrite arm spacing gives values larger than the distance defined for a converging GB by the first criterion, so that it satisfies the two criteria.

In the present article, we propose an advanced thermo-hydraulic model dedicated to welding simulation associated to grain structure prediction using the CAFE method. Analyses are developed for the Gas Tungsten Arc Welding (GTAW) process applied to the 316 L steel grade without addition of metal. The macroscopic comparison of melt pool shape, fluid flow velocity and weld bead shape after solidification are made possible by the development of a test bench dedicated to welding observations [28]. Comparisons of simulated grain structures are carried out with EBSD maps on large surfaces of specific samples. The chaining and coupling schemes of the CAFE model are both applied in order to quantitatively evaluate their impact on the predicted grain structures.

Table 1
Welding parameters.

Parameter	Value		Unit
	V_1	V_2	
Welding voltage, U	8.76	8.67	V
Current intensity, I	81.3	81.5	A
Efficiency, η	0.65	0.6	–
Welding speed	3.3	4.3	mm s^{-1}
Welding length	100		mm
Start point of welding	$(X, Y, Z) = (20, \ 0, \ 1.5)$		mm

The material and the experimental setup are first presented, followed by the model description and the simulation results. At last, the influence of the different modeling approaches is discussed.

2. Experimental and material

2.1. Experimental set-up

The experimental device designed to carry out full penetration welding on sheet-metal plates is available in reference [28]. The device has a static heat input in the laboratory reference frame in order to ease the observation. It is composed of a GTAW station with arc voltage and welding current measurement systems. A mobile support is used with controlled motion speed. It is made of an open rectangular metallic stand with dimensions 150 × 75 × 1.5 mm closed at its top by the sheet-metal plate that serves as sample coupon and at its bottom by a glass plate. The volume encompassed between these elements creates a gas chamber continuously filled with argon for protection from air oxidation of the lower side of the weld pool. Similarly, an argon flow rate of 15 L/min is applied during processing through the static welding torch in order to protect the upper side of the weld pool (Fig. 1(b)). A static camera (Mako model from Allied Vision Technologies), labelled *AVT Camera* in Fig. 1(a), offers a global view of the weld pool from its lower side through the glass plate at 300 frames per second. The region of interest is illuminated by a 15 W laser diode that is fixed at the lower side of the metal plate. Thanks to the differences of reflection between solid and liquid parts, liquid zones can be identified, and it is possible to measure the size and shape of the melt pool and to estimate fluid flow by following the trajectories of floating particles at the molten metal/gas interface. Welding is carried out along the X direction by moving the mobile support in the opposite direction at velocity V. The vertical direction through the thickness of the metal plate is Z so the complementary transverse direction of the reference frame is Y as presented in Fig. 1. The origin of the system, labelled O, is chosen at the center of the lower surface of the plate.

The arc is initiated by lift-arc in a motionless configuration at the beginning of the experiment and the support begins to move 0.4 s after. The sample coupon dimensions are 150 × 75 × 1.5 mm. Values of welding parameters are chosen to obtain fully penetrated weld pool; they are given in Table 1. Two welding speeds are investigated, referred to as $V_1 = 3.3$ mm s^{-1} and $V_2 = 4.3$ mm s^{-1}. By modulating the welding speed, we expect variations of the weld pool dimensions and the shape of the solidification interface by the change of heat transfer and fluid flows motions. It is worth noting that the welding parameters, i.e. the welding voltage and the current intensity, are maintained constant for the two reported experimental configurations so as to ease comparisons. The total welding length is 100 mm. This was found sufficient to reach a steady regime for the melt pool shape over a sufficiently large distance, i.e. an established and fixed melt pool shape in the reference associated to the camera. The measures are carried out during the last 35 mm excluding the arc extinction stage.
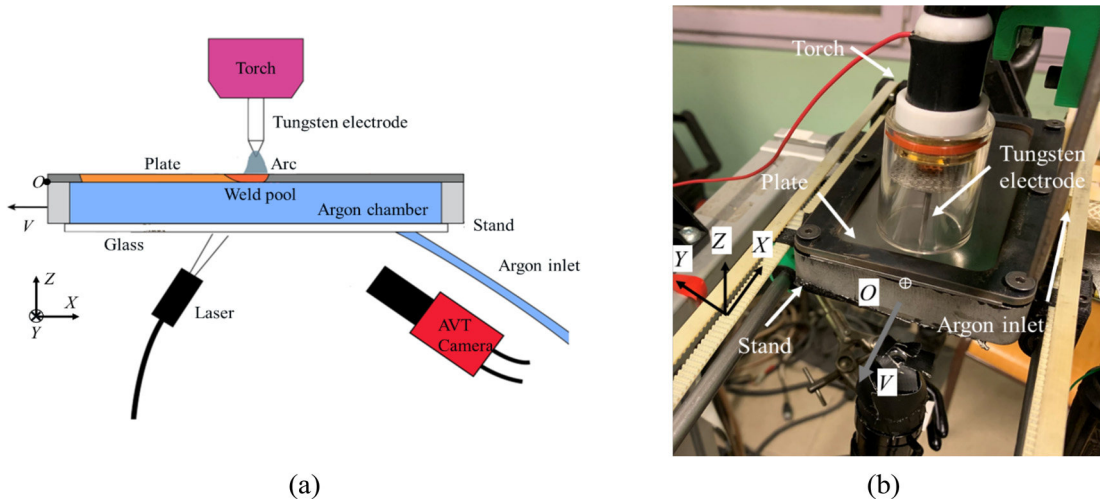
Fig. 1. Experimental setup with (a) schematics of the various devices including diagnostics apparatus and metal plate sample and (b) picture of the GTAW torch and stand of the sample.

Table 2
Chemical composition of 316 L steel (according to EN10088–4 [29]).

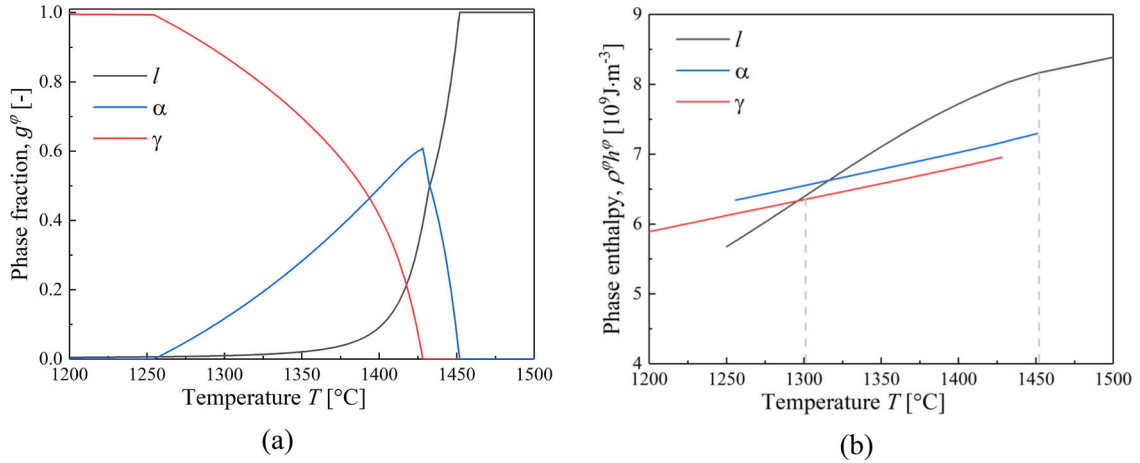| Fe	C	Cr	Mn	Mo	Ni	P	S	Si	N	Co	Unit
balanced	0.016	16.765	1.383	2.044	10.070	0.031	0.001	0.389	0.041	0.187	wt%

Fig. 2. Temperature evolution of (a) the volume fraction of the phases involved during solidification, g^φ with $\varphi = \{l, \alpha, \gamma\}$, corresponding to liquid, l, ferrite, α, and austenite, γ, and (b) their volumetric enthalpy, $\rho^\varphi h^\varphi$ [34].
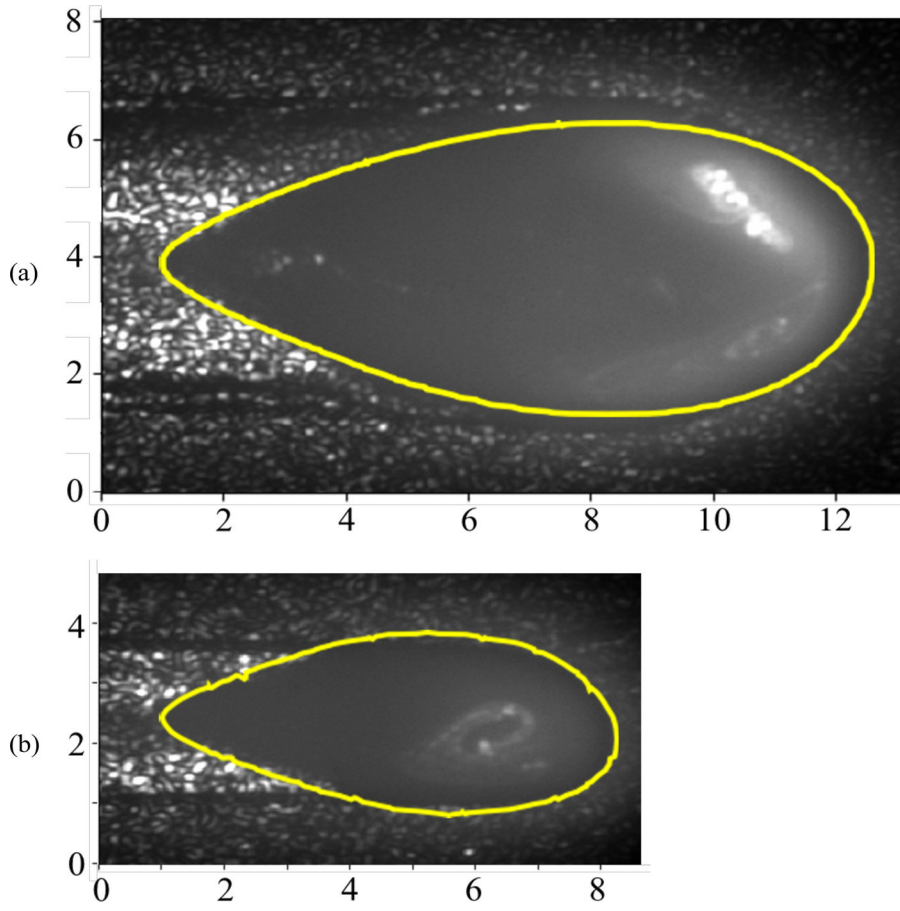
2.2. Material

The 316L stainless steel is used, with chemical composition reported in Table 2. Fig. 2(a) describes the transformation path computed with the TCFE9 thermodynamic database [30] assuming partial equilibrium during solidification [31] with activation of the peritectic reaction where liquid, l, and ferrite, α, transform into austenite, γ. It shows the evolution with temperature, T, of the volume fraction of phases, g^φ with $\varphi = \{l, \alpha, \gamma\}$. Upon cooling, solidification starts at the liquidus temperature, $T_L = 1452°C$, and ends at the solidus temperature, $T_S = 1301°C$. The latter value is chosen for a remaining fraction of liquid lower than 1%. No other thermodynamic phases have been considered in the simulation. The remaining fraction of ferrite is $g^\alpha = 13\%$. The choice of the partial equilibrium solidification path is motivated by experimental observations showing that austenite is dominant at room temperature after completion of solidification [32,33]. Yet a full equilibrium lever rule transformation path predicts that ferrite is the dominant phase at room temperature as austenite resulting from the peri-

tectic reaction retransforms into ferrite at low temperature, reaction being prevented by the high cooling inherent to the present welding process. At the same time, a Gulliver-Scheil approximation cannot predict the peritectic transformation [31]. So, the partial equilibrium solidification path with peritectic transformation seems the more reasonable approximation. Tabulations of the volumetric enthalpies are also extracted at the corresponding temperature and phase composition by multiplying the density, ρ^φ, by the enthalpy per unit mass, h^φ, for all phases $\varphi = \{l, \alpha, \gamma\}$ using the PhysalurgY library [34]. Besides, the thermal conductivity $\langle\kappa\rangle^\varphi$ for all phases $\varphi = \{l, \alpha, \gamma\}$ is expressed by the relationship $\langle\kappa\rangle^\varphi = 0.0143T + 13.803$ W m^{-1} K^{-1} for T within the interval [20, 1400]°C [35].

2.3. In-situ observations and characterizations

Characterizations are first conducted by analyses of the in-situ video recording of the melt pool by the camera. More than two thousand frames per experiment are analyzed in order to extract the evolution

Fig. 3. Surface melt pool as recorded by video imaging at the bottom surface of the samples for welding speed (a) V_1 and (b) V_2 (see Table 1). Scales in mm [28].

of weld pool geometry. Little variations in shape can be noted, probably due to fluctuations of heat and fluid flow, expressing the dynamics of the weld pool. Based on these data, it is possible to define an average weld pool contour during this quasi-steady state.
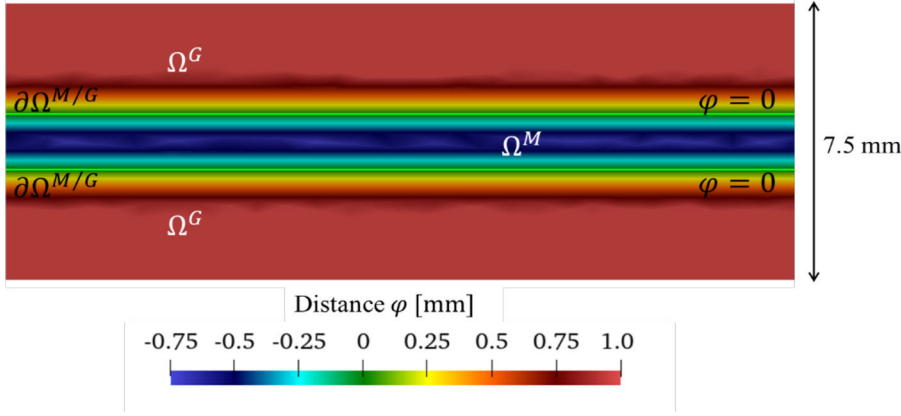
Fig. 3 presents the steady shape of the melt pool at established welding regimes for speeds V_1 and V_2 as observed on the bottom surface of the plate. The contrast and the reflection of the light is sufficient to clearly distinguish between the surface of the molten metal, with a smooth distribution of gray levels, and the solid-containing regions where modulations of gray color appear due to surface roughness. The contour of the molten pool can thus be highlighted in yellow in Fig. 3. A typical teardrop shape is observed, with smaller dimensions as welding speed increases while maintaining constant voltage and current (see Table 1). The liquid metal velocity is also evaluated thanks to visible moving particles at the surface of the melt pool. The particles trajectories are obtained by the PTV method [36]. The direction of liquid circulation can be evaluated and the velocities of the particles are obtained by the time derivative of their positions. The PTV method reveals a fluid flow from the center towards the border of the melt pool, typical of surface tension driven convection with a negative Marangoni coefficient. More details on the experimental setup, in-situ diagnostics techniques and exploitation methodologies are available in reference [28]. postmortem metallography is also achieved in transverse cross sections of the weld bead. This gives access to the weld bead profile and measurement of its vertical deflection, due to the effect of gravity while the metal is in the liquid state. Consequently, polishing is required in order to prepare the samples for EBSD measurements conducted in XY planes along the top surface of the plate. Beside the texture of the grain structure produced upon solidification, EBSD gives access to the initial grain structure in base metal. This includes both the texture and the density the latter being estimated to $6.4 \cdot 10^{13}$ grains per cubic meter.

3. Modeling

The present model is first based on FE solutions for heat and mass transfer within a composite domain Ω made of metal (M) plus gas (G) subdomains, respectively Ω^M and Ω^G, with metal/gas boundary[1] $\partial\Omega^{M/G}$. The metal is composed of the liquid and solid phases of 316 L alloy, as listed above. The CA method is also used for the description of the grain structure, i.e. its initial state prior to welding, its melting due to heating by the torch and its solidification after the torch has moved away. The mass, energy and momentum conservation equations are solved simultaneously on the composite domain described by a FE mesh. The initial configuration is a three-dimensional rectangular metallic subdomain of thickness representing the full metal plate sandwiched by two disconnected layers composing the gas subdomain. A LS method is used to compute the evolution of the top and bottom metal boundaries with the gas, hence the resulting deflection of the weld bead due to melting and solidification. The fields computed on the adapted FE mesh are projected on a fixed and coarser mesh, hereafter referred to as CA mesh. The latter is used to build a regular lattice of cubic cells, referred to as CA grid. Section 3.4 explains the reasons for such a multiple mesh and grid strategy and a detailed description with illustrations is given by Chen et al. [14,15].

In the simulation, the heat source is moved from coordinates $X = 20$ mm to $X = 69.5$ mm, i.e. over a 50 mm length, and at mid-width of the plate ($Y = 0$ mm) at a constant velocity. Note that this differs from the experimental configuration in which the heat source is fixed and

---

[1] The word « boundary » is preferred to the word « interface » as the separation between the metal and the gas can be the result of several combined interfaces (e.g., liquid metal – gas plus solid metal – gas in the solidification interval, with solid made of several phases as shown in Fig. 2).

Fig. 4. Cross section through the simulation domain normal to the initially planar sheet plate revealing the LS function φ defining (green horizontal lines) the boundary $\partial\Omega^{M/G}$ between the metal subdomain, Ω^M, and the gas subdomain, Ω^G, by iso-value $\varphi = 0$, capped to the maximum value $\varphi = 1$ mm in the gas subdomain.

the sample moves, yet being fully equivalent. The heat source is located above the upper surface of the plate, $Z > 1.5$ mm.

3.1. Metal/gas boundary

The LS function φ represents the signed distance between any given point of the simulation domain and the metal/gas boundary. As illustrated in Fig. 4, the region $\varphi < 0$ (resp. $\varphi > 0$) is associated with the metal (resp. gas) subdomain. Initially planar, the metal domain is 1.5 mm thick and the surrounding air layers are 3 mm thick, explaining the total 7.5 mm scale of the simulation domain in Fig. 4. The figure also reveals that the function φ is confined within limits $[-0.75, 1]$ mm. This optimization reduces the computing time of the distance function while not modifying the description of the boundary and its evolution.

Consequently, the top and bottom boundaries of the metal subdomain are located by the iso-value $\varphi = 0$ mm at any time during the simulation. The smoothed Heaviside function $\mathcal{H}^M(\varphi)$ is defined to continuously evolve over a distance 2ε, from 1 in the metal subdomain, for $\varphi < -\varepsilon$, to 0 in the gas subdomain, for $\varphi > +\varepsilon$, so that ε represents the half-thickness of the transition zone between subdomains:

$$\mathcal{H}^M(\varphi) = \begin{cases} 1 & \text{if } \varphi < -\varepsilon \\ 0 & \text{if } \varphi > +\varepsilon \\ \frac{1}{2}\left(1 + \frac{\varphi}{\varepsilon} + \frac{1}{\pi}\sin\left(\frac{\pi\varphi}{\varepsilon}\right)\right) & \text{if } |\varphi| \le +\varepsilon \end{cases} \quad (1)$$

Hence, $\mathcal{H}^M$ and $\mathcal{H}^G = 1 - \mathcal{H}^M$ are the presence functions in the metal and gas subdomains, respectively, with φ-dependency dropped for simplicity. One can then directly generalize a property ξ at any point of the simulation domain by the arithmetic mean $\widehat{\xi}$:

$$\widehat{\xi} = \mathcal{H}^M \xi^M + \mathcal{H}^G \xi^G \quad (2)$$

where ξ^M and ξ^G denote the properties respectively in the metal and gas subdomains. The transition zone between subdomains is a layer surrounding the iso-value $\varphi = 0$ mm defined in the interval $\varphi \in [-\varepsilon, +\varepsilon]$. Thus, ε is a parameter that needs to be chosen very small compared with the characteristic dimensions of the subdomains. The use of the smoothed Heaviside function avoids an abrupt change of the properties through the subdomain boundaries and facilitates the numerical solution of the conservation equations solved as a monolithic system in the whole simulation domain.

Forces act on the metal/gas boundary defined by the iso-value $\varphi = 0$ mm, contributing to its spatial and temporal evolution. However, it is not convenient to impose a condition on the surface $\partial\Omega^{M/G}$ defined by $\varphi = 0$. Instead, Brackbill et al. [37] introduced the Continuum Surface Force (CSF) method to transform any surface load, defined by a surface force F, into a volume force loading:

$$\int_{\partial\Omega^{M/G}} F \, dS = \int_{\Omega} F\delta \, dV \quad (3)$$

where δ is the derivative of the Heaviside function $\mathcal{H}^M$ with respect to the LS function φ and $\Omega = \Omega^M \cup \Omega^G$ is the whole simulation domain. According to equation (1), δ is thus a smoothed Dirac function with zero value outside the transition zone $[-\varepsilon, +\varepsilon]$ and it takes the expression $(1 + \cos(\pi\varphi/\varepsilon))/(2\pi)$ in the transition zone. The equivalent volumetric contribution $F\delta$ added to the whole simulation domain Ω thus only acts around the boundary $\partial\Omega^{M/G}$ to impose the nominal surface force F. The CSF method can be applied for both scalar and vector fields to introduce boundary conditions as source terms in the FE method.

In a time-stepping loop, the level set function is updated to model the movement of the metal/gas boundary due to fluid flow. The evolution of the distance function is computed by solving the transport equation:

$$\frac{\partial\varphi}{\partial t} + \widehat{\langle \boldsymbol{v^F} \rangle} \cdot \nabla\varphi = 0 \quad (4)$$

$$\widehat{\langle \boldsymbol{v^F} \rangle} = \mathcal{H}^M g^l \langle \boldsymbol{v} \rangle^l + \mathcal{H}^G \langle \boldsymbol{v} \rangle^a \quad (5)$$

where t is the time and $\widehat{\langle \boldsymbol{v^F} \rangle}$ is the average fluid velocity defined over the whole domain using equations (1) and (2), i.e. averaged over both the liquid, l, of the metal subdomain, M, and the air phase, a, of the gas subdomain, G. In equation (5), g^l is the volume fraction of liquid and $\langle \boldsymbol{v} \rangle^l$ and $\langle \boldsymbol{v} \rangle^a$ are the velocities of the liquid and gas phases, respectively. The average fluid velocity is determined by solving the mass and momentum conservation equations as presented in section 3.3 . However, because such transport does not preserve the Eikonal property (unitary gradient vector) of the level set function, Shakoor et al. [38] developed a reinitialization method based on the geometrical computation of the distance function between each FE node and the transported zero level set boundary. This direct reconstruction of φ is performed after each transportation step of the level set function.

3.2. Energy conservation

The standard volume averaging method [39–41] is applied to the conservation of energy over the metallic subdomain as it is composed of the several thermodynamic phases shown in Fig. 2. This is not needed for the gas subdomain as it is made of a single argon gas phase, a, so $G \equiv a$ and its volume fraction in the gas subdomain is simply $g^a = 1$. The fluids, F, made of the liquid metal plus the gas, are the only moving phases. In other words, the solid metallic phases, α and γ, are both assumed fixed. Further assuming that the fluids are incompressible, the average energy conservation equation becomes:

$$\frac{\partial\widehat{\langle \rho h \rangle}}{\partial t} + \widehat{\langle \boldsymbol{v^F} \rangle} \cdot \nabla\widehat{\langle \rho h \rangle}^F = \nabla \cdot \left(\widehat{\langle \kappa \rangle}\nabla T\right) + \dot{Q} \quad (6)$$

with:

$$\widehat{\langle \rho h \rangle} = \mathcal{H}^M \left(g^l \langle \rho \rangle^l \langle h \rangle^l + g^\alpha \langle \rho \rangle^\alpha \langle h \rangle^\alpha + g^\gamma \langle \rho \rangle^\gamma \langle h \rangle^\gamma\right) + \mathcal{H}^G \langle \rho \rangle^a \langle h \rangle^a \quad (7)$$
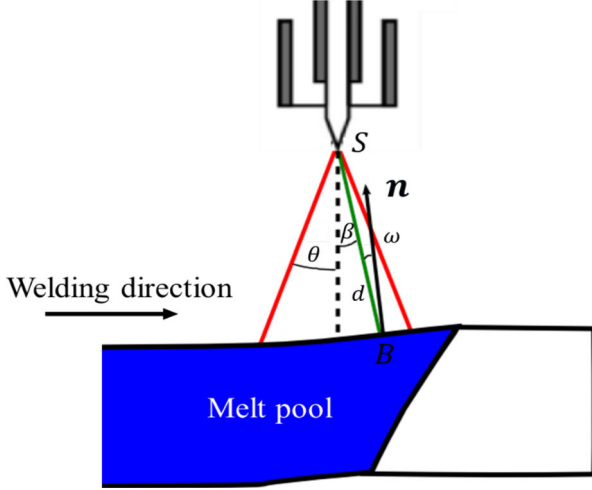
Fig. 5. Definitions of the heat source distribution in plasma arc welding.

$$\widehat{\langle\rho h\rangle^F} = \mathcal{H}^M \langle\rho\rangle^l \langle h\rangle^l + \mathcal{H}^G \langle\rho\rangle^a \langle h\rangle^a \tag{8}$$

$$\widehat{\langle\kappa\rangle} = \mathcal{H}^M \left(g^l \langle\kappa\rangle^l + g^\alpha \langle\kappa\rangle^\alpha + g^\gamma \langle\kappa\rangle^\gamma\right) + \mathcal{H}^G \langle\kappa\rangle^a \tag{9}$$

where $\widehat{\langle\rho h\rangle}$ is the average volumetric enthalpy over all subdomains and phases according to Eq. (7), i.e. introducing the average volumetric enthalpy of the metal subdomain $\langle\rho h\rangle^M = g^l \langle\rho\rangle^l \langle h\rangle^l + g^\alpha \langle\rho\rangle^\alpha \langle h\rangle^\alpha + g^\gamma \langle\rho\rangle^\gamma \langle h\rangle^\gamma$ and of the gas subdomain $\langle\rho h\rangle^G = \langle\rho\rangle^a \langle h\rangle^a$, where g^φ, $\langle\rho\rangle^\varphi$ and $\langle h\rangle^\varphi$ are the volume fraction, density and mass enthalpy of phase φ ($\varphi = \{l, \alpha, \gamma, a\}$), respectively. The same principle applies for the average thermal conductivity in the metal subdomain, $\langle\kappa\rangle^M = g^l \langle\kappa\rangle^l + g^\alpha \langle\kappa\rangle^\alpha + g^\gamma \langle\kappa\rangle^\gamma$ and in the gas subdomain, $\langle\kappa\rangle^G = \langle\kappa\rangle^a$ where $\langle\kappa\rangle^\varphi$ is the thermal conductivity of phase φ ($\varphi = \{l, \alpha, \gamma, a\}$), respectively. Only the energy over the liquid metal and the argon gas, $\widehat{\langle\rho h\rangle^F}$, is transported at velocity $\widehat{\langle v^F\rangle}$, equation(5).

In this work, an adiabatic boundary condition is applied at the limits of the quadrangular simulation domain encompassing the metal plate sandwiched by the top and bottom gas layers. The volumetric heat source in the right-hand-side of Eq. (6), $\dot{Q}$, represents the arc plasma heating the workpiece. It is described by a Gaussian angular heat source as initially proposed by Desmaison [42] and exploited by Chen [14,15]:

$$\dot{Q} = \delta \frac{3\dot{Q}_{Plasma}}{K_P \, 2\pi \, d^2 \, (1 - \cos\theta)} \exp\left(-3\left(\frac{\beta}{\theta}\right)^2\right) \cos\omega \tag{10}$$

with $\dot{Q}_{Plasma}$ the effective power of the plasma arc of aperture angle θ as defined in Fig. 5. Eq. (10) is valid for any point B located at the upper surface of the metal/gas boundary. This point is defined by its half-angle, β, between SB and the heat source direction (dashed line), necessarily smaller than θ, its distance d from the origin of the heat source, S, and the angle ω between SB and the local normal $n = \nabla\varphi$ (as $\|\nabla\varphi\| = 1$) of the metal/gas boundary. The normalization factor K_P is introduced to ensure that the requested effective power is well retrieved by an energy balance:

$$K_P = 0.95 + 0.0347 \, \theta^2. \tag{11}$$

Details on the numerical implementations of the FE energy solver using tabulated properties and solidification paths are given in reference [43].

3.3. Fluid mechanics

The fluid flow evolutions in the liquid domain are limited in the melt pool and in the mushy zone. Fluid dynamics equations are established by

Table 3
Properties used for the simulations for the 316 L steel grade and the argon gas.

Property	Variable	Value	Unit
Marangoni coefficient	$\partial\gamma_s/\partial T$	$-8 \cdot 10^{-4}$	N m^{-1} K^{-1}
Surface tension [47]	γ_s	1.943	N m^{-1}
Metal density	$\rho^\varphi, \varphi = \{l, \alpha, \gamma\}$	7800	kg m^{-3}
Gas density	ρ^a	1.3	kg m^{-3}
Liquid metal dynamic viscosity	μ^l	$5 \cdot 10^{-2}$	Pa s
Solid metal dynamic viscosity	$\mu^\varphi, \varphi = \{\alpha, \gamma\}$	1000	Pa s
Gas dynamic viscosity	μ^a	$5 \cdot 10^{-3}$	Pa s
Gas thermal conductivity	$\langle\kappa\rangle^a$	1	W m^{-1} K^{-1}

the mass and momentum conservation equations (Navier-Stokes) [44]:

$$\begin{cases} \nabla \cdot \widehat{\langle v^F\rangle} = 0 \\ \widehat{\rho^F}\left(\frac{\partial \widehat{\langle v^F\rangle}}{\partial t} + \frac{1}{g^F}\nabla \cdot \left(\widehat{\langle v^F\rangle} \times \widehat{\langle v^F\rangle}\right)\right) = \nabla \cdot \langle \overline{\overline{=}}\sigma^F\rangle + \widehat{\rho g} + F_s \end{cases} \tag{12}$$

The stress tensor is $\langle \overline{\overline{\sigma}}^F\rangle = 2\hat{\mu}\langle\overline{\overline{\dot{\varepsilon}}}^F\rangle - \langle p^F\rangle\overline{\overline{I}}, \langle\overline{\overline{\dot{\varepsilon}}}^F\rangle = (1/2)(\nabla \cdot \widehat{\langle v^F\rangle} + (\nabla \cdot \widehat{\langle v^F\rangle})^T)$, $\langle p^F\rangle = g^F p$. p is the pressure, g^F is the fluid fraction defined as an arithmetic mixing between liquid metal and argon gas Eq. (13), $\hat{\mu}$ and $\widehat{\rho^F}$ present the average viscosity and density over all fluid subdomains (liquid metal and argon gas) according to Eq. (14), ((15) respectively. And $\widehat{\rho g}$ expresses the gravity applied to the fluid as presented by Eq. (16).

$$g^F = \mathcal{H}^M g^l + \mathcal{H}^G g^a = \mathcal{H}^M g^l + \mathcal{H}^G. \tag{13}$$

$$\hat{\mu} = \mathcal{H}^M \langle\mu\rangle^M + \mathcal{H}^G \mu^a \tag{14}$$

$$\widehat{\rho^F} = \mathcal{H}^M \langle\rho\rangle^l + \mathcal{H}^G \langle\rho\rangle^a \tag{15}$$

$$\widehat{\rho g} = \mathcal{H}^M g^l \langle\rho\rangle^l g + \mathcal{H}^G \langle\rho\rangle^a g \tag{16}$$

F_s denotes the surface force applied to the metal/gas boundary. In the GTAW process, the surface force is associated with surface tension F_s^T and the Marangoni force F_s^M. The recoil pressure is neglected in GTAW process, due to the low power density compared with laser welding or additive manufacturing [45].

$$F_s = F_s^T + F_s^M \tag{17}$$

$$\begin{cases} F_s^T = \delta\gamma_s\kappa_t n \\ F_s^M = \delta\nabla_s\gamma_s = \delta\frac{\partial\gamma_s}{\partial T}\nabla_s T \end{cases} \tag{18}$$

γ_s is the liquid-gas surface tension, $\kappa_t = -\nabla \cdot n$ is the total curvature with n the unit normal vector pointing out of liquid: $n = \nabla\varphi$ ($\|\nabla\varphi\| = 1$). ∇_s denotes the surface gradient operator. Accordingly, $\nabla_s T$ is the component of the temperature gradient which is tangent to the boundary: $\nabla_s T = \nabla T - (\nabla T \cdot n)n$. The surface tension γ_s is assumed to depend only on temperature, so that $\nabla_s\gamma_s$ is simply the product of the tangential temperature gradient by the Marangoni coefficient $\partial\gamma_s/\partial T$, which is seen as a characteristic property of the liquid metal. Thus, the sign of $\partial\gamma_s/\partial T$ directly influences the direction of the convection flow along the liquid metal boundary, and thereafter in the whole liquid domain. Consequently, the temperature distribution and the shape of the melt pool are mainly associated with the Marangoni force distribution [46].

Other 316 L steel grade properties used in the simulations are listed in Table 3. It should be noted that the Navier-Stokes equations, Eq. (12), are solved on the whole domain, that is for gas, liquid and solid metal. Having in mind that the main objective of the mechanical resolution is to predict fluid flow in the melt pool, this justifies i) the use of a

Table 4
Dendrite tip kinetics law.

K_1	$v_1^{\langle 100 \rangle} = 1.8 \cdot 10^{-6} \Delta T^{2.7}$	mm s^{-1}
K_2	$v_2^{\langle 100 \rangle} = 1.01 \cdot 10^{-3} \Delta T^{3.26} + 1.32 \cdot 10^{-6} \Delta T^{5.19}$	mm s^{-1}

Newtonian behavior (and Navier-Stokes equations) in the solid, as the objective is not to address the plastic deformation of the solid metal, and ii) the use of viscosity values that will be the nominal one in the liquid metal, but that could be arbitrarily adjusted in the gas and the solid. Those arbitrary values should comply with two constraints: the solution velocities in the solid should be small enough, compared to the liquid velocities, and the global viscosity range should be as small as possible, in order to allow a rapid convergence of the iterative solvers in charge of the resolution of the linear sets of equations. Therefore, as indicated in Table 3, the viscosities of solid phases are identically chosen equal to 1000 Pa s, while the gas viscosity is chosen 10 times smaller than the liquid viscosity, as the present model does not aim at a quantitative prediction of gas flow. Finally, Eq. (14) is used to model the viscosity change within the metal/gas interfacial region, while the viscosity change between solid and liquid is modelled by the following logarithmic mixing rule: $\langle \mu \rangle^M = (\mu^l)^{g_{n,FE}^l}(\mu^\alpha)^{g_{n,FE}^\alpha} (\mu^\gamma)^{g_{n,FE}^\gamma}$. Taking the same dynamic viscosity value for both solid phases, $\mu^s = \mu^\alpha = \mu^\gamma$, one can rewrite $\langle \mu \rangle^M = (\mu^l)^{g_{n,FE}^l}(\mu^s)^{(1-g_{n,FE}^l)}$.

3.4. Grain structure

The CA method is used to model the grain structure. The principle is well documented in the literature and is only briefly explained hereafter following the work by Chen et al. applied to welding processes [14,15]. The CA grid is made of a regular lattice of cubic cells distributed over a finite element mesh, hereinafter referred to as the CA mesh. Neither the CA grid not the CA mesh evolve during the simulation so the position of a CA cell is uniquely defined within the CA mesh. The CA mesh is encompassed within a larger simulation domain used to solve the equations previously introduced. The latter simulation domain is referred to as FE mesh. It dynamically evolves during the simulation to track the metal/gas boundary and to adapt to the changes of temperature gradient and heat source position. Quantities computed onto the FE mesh (e.g., the level set function, φ, the temperature, T, the velocity of the fluid, $\widehat{\langle v^F \rangle}$, …) can be transported onto the CA mesh and then further interpolated at the center of the CA cells. This was found much more efficient than recomputing the CA cell position within the FE mesh. Each cell is attributed a state index: gas or metal according to the sign of the level set function, but also liquid, part of the growing mushy zone or fully developed mushy zone and/or solid. When not gas nor liquid, a cell is an elementary brick of a single grain defined by a crystallographic orientation, i.e., the three Euler angles (φ_1, ϕ, φ_2) in the Bunge convention. Rules define the evolution of the state index as a function of the neighboring cells state index and interpolated quantities at the CA cells deduced from the FE solutions. Melting and growth are thus modeled. For melting, a cell that was part of the metal with a temperature higher than the liquidus temperature is simply switched to the corresponding liquid state index. For growth, a dedicated algorithm is applied to the cells that are part of the mushy zone and have at least one neighboring liquid cell. It assumes that primary solidification takes place with a dendritic microstructure along the main $\langle 100 \rangle$ crystallographic directions. A continuously increasing function of the velocity, $v^{\langle 100 \rangle}$, with the undercooling, ΔT, is used. In the following simulations, two such functions are tested, $v_1^{\langle 100 \rangle}(\Delta T)$ and $v_2^{\langle 100 \rangle}(\Delta T)$, that are listed in Table 4 and referred to as K_1 and K_2, respectively. Coefficient K_1 is adjusted in order to retrieve the position of the growth front observed in Fig. 3 for both welding speeds V_1 and V_2. For comparison, the second dendrite tip kinetics law, K_2, is deduced from a model proposed in the literature for a multicomponent alloy [48–50] as detailed later in Section 5.1 . The influence of the growth laws on grain structure is also discussed in Section 5.1 .

Two coupling schemes are used in the simulations that are summarized in Fig. 6: chaining and coupling. The main difference relies on communications between the CA and FE methods and the resulting solution of the energy conservation. The chaining scheme simply makes use of the temperature field computed on nodes n of the FE mesh, $T_{n,FE}$, projected on nodes n of the CA mesh, $T_{n,CA}$, and then interpolated on cell v of the CA grid, $T_{v,CA}$. Based on this temperature field, the growth velocity of the grain envelope along the $\langle 100 \rangle$ directions, $v^{\langle 100 \rangle}(\Delta T_{v,CA})$, is therefore computed. The temperature field itself, $T_{n,FE}$, is computed using the uniquely defined solidification path given in Fig. 2(a): the fraction of the thermodynamic phases $g_{n,FE}^\varphi$ with $\varphi = \{l,\ \alpha,\ \gamma\}$ uniquely depends on the temperature, $g^\varphi(T_{n,FE})$, as given by the tabulation presented in Fig. 2(a). The coupling scheme is more sophisticated as the fraction of the phases now depends on the presence of the grains, or fraction of mushy zone, $g_{n,FE}^m$. The latter is first computed by considering the growth envelope associated to each cell v of the CA grid, $g_{v,CA}^m$, then fed back to nodes n of the CA mesh, $g_{n,CA}^m$, and finally projected to nodes n of the FE mesh, $g_{n,FE}^m$, so that the fraction of phases becomes $g_{n,FE}^\varphi = g_{n,FE}^m\ g^\varphi(T_{n,FE})$ with $\varphi = \{l,\ \alpha,\ \gamma\}$. Thus, the temperature becomes a function of the presence of the grains. This coupling scheme is required when the temperature field is expected to depend on the development of the microstructure [10,51,52].

3.5. Numerical parameters

Fig. 7 presents a section through the simulation domain that corresponds to a central longitudinal cut ($Y = 0$) through the weld bead at a given time. The tetrahedral FE mesh is displayed. It reveals the meshing strategy adopted, with parameters summarized in Table 5. The mesh size within the transition zone between subdomains is one-fifth of the half-transition zone thickness ϵ, the latter being much smaller than the subdomain dimensions. As expected, the boundaries $\partial \Omega^{M/G}$, computed by the iso-value $\varphi = 0$ (green contours), falls within this region of very fine meshes. A cylindrical zone (yellow contour) with fixed mesh size 0.5 mm is centered below the mobile heat source and remain uniform in the gas and in the regions away from the melt pool. Also show in Fig. 7 is the anisotropic mesh outside the cylindrical zone, with small dimension along the Z-direction (0.4 mm) compared to the other directions (1 mm) in the gas subdomain. Very far from the melt pool (not shown here), the mesh size is uniform with a coarser size (1.5 mm) so as to save computation time. Also note the refined mesh dimensions at the boundaries of the melt pool. Indeed, the gradient variation of the liquid fraction is calculated from element to element during the simulation. Its interpolation error being evaluated, a desired edge length of each element is deduced so as to minimize the total interpolation error [53]. While the FE mesh is adapted during the simulation, the CA mesh is fixed, with constant mesh size given in Table 5. Its dimensions include the whole thickness of the metal sheet but only a thin layer of the gas subdomain, hence its total thickness 1.8 mm. Similarly, it is chosen shorter in the X and Y directions. The reason is that no conservation equations are solved onto this mesh that only serves to communicate FE fields deduced from the solutions computed at the FE mesh, as explained above. Consequently, the dimensions of the CA mesh must only cover the regions where the grain structure simulation is targeted. The CA grid is indeed built based on the CA mesh. The size of the cells of the CA grid is chosen small enough to represent the grain structure of the base metal considering both its size and texture. With a grain size of the order of 25 μm, the cell size is fixed to 20 μm. The volume of the CA mesh being 40 × 7 × 1.8 = 504 mm^3, the total number of cells composing the CA grid is 63 millions. Each simulation is distributed amongst 56 processors bullx R424 Intel Xeon E5-2680 v4 with 128 Go RAM based on an in-house C++ programming language code developed at the CEMEF research center, with a typical simulation time of 20 hours including FE solutions of all equations listed
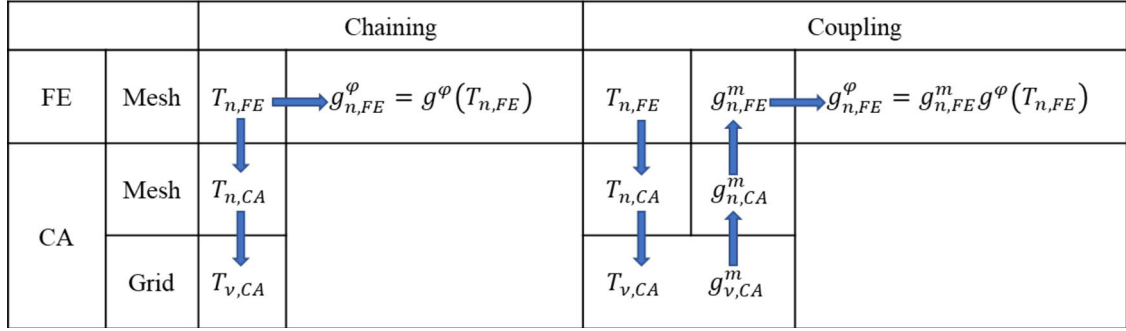
		Chaining		Coupling		
FE	Mesh	$T_{n,FE}$ → $g^{\varphi}_{n,FE} = g^{\varphi}(T_{n,FE})$		$T_{n,FE}$	$g^{m}_{n,FE}$ → $g^{\varphi}_{n,FE} = g^{m}_{n,FE} g^{\varphi}(T_{n,FE})$	
CA	Mesh	$T_{n,CA}$		$T_{n,CA}$	$g^{m}_{n,CA}$	
	Grid	$T_{v,CA}$		$T_{v,CA}$	$g^{m}_{v,CA}$	

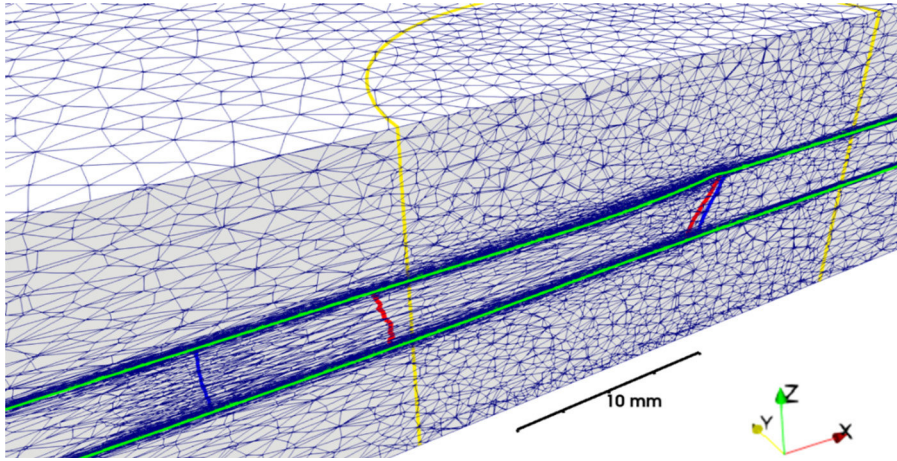**Fig. 6.** Chaining and coupling strategies developed for the CAFE model and applied in the simulations of GTAW process, $\varphi = \{l, \alpha, \gamma\}$.

Fig. 7. Snapshot of the FE mesh at the top surface and in a cross section of the simulation domain illustrating the distribution of mesh size used to solve equations (6) to (18), also revealing (green) the location of the metal/gas boundaries. The (red line) liquidus temperature and (blue line) solidus temperature are drawn in the central longitudinal cross section through the weld bead. The (yellow) cylindrical contour through the entire domain thickness and the top surface identifies the region below the heat source where the mesh size is refined (see Table 5).

Table 5
Mesh parameters of the simulations.

	Dimensions	Value (mm)
FE mesh	Domain size	150 $(X) \times$ 75 $(Y) \times$ 7.5 (Z)
	Half-transition thickness ϵ	0.1
	Mesh size in the transition zone	0.02
	Mesh size below the heat source	0.5
	Mesh size in the heat affected zone	1 (X), 1 (Y), 0.4 (Z)
	Mesh size elsewhere	1.5
CA mesh and grid	Domain size	40 $(X) \times$ 7 $(Y) \times$ 1.8 (Z)
	Mesh size	0.2
	Cell size	0.02

above, remeshing, transfer of information between meshes and grid, CA algorithms, input/output on hard drive, …

4. Simulation results

In the following section, simulations with the coupling scheme are presented, for the two welding configurations V_1 and V_2 reported in Table 1. This is done using the dendrite tip kinetics law K_1. These two simulations are hereafter referred to as cases V_1K_1CO and V_2K_1CO. Comparisons are conducted considering the melt pool shape observed by the AVT camera and the measured texture of the grain structure as deduced from EBSD measurements. Results will serve for comparison with three additional simulations reported in the following. All configurations of the simulations are summarized in Table 6.

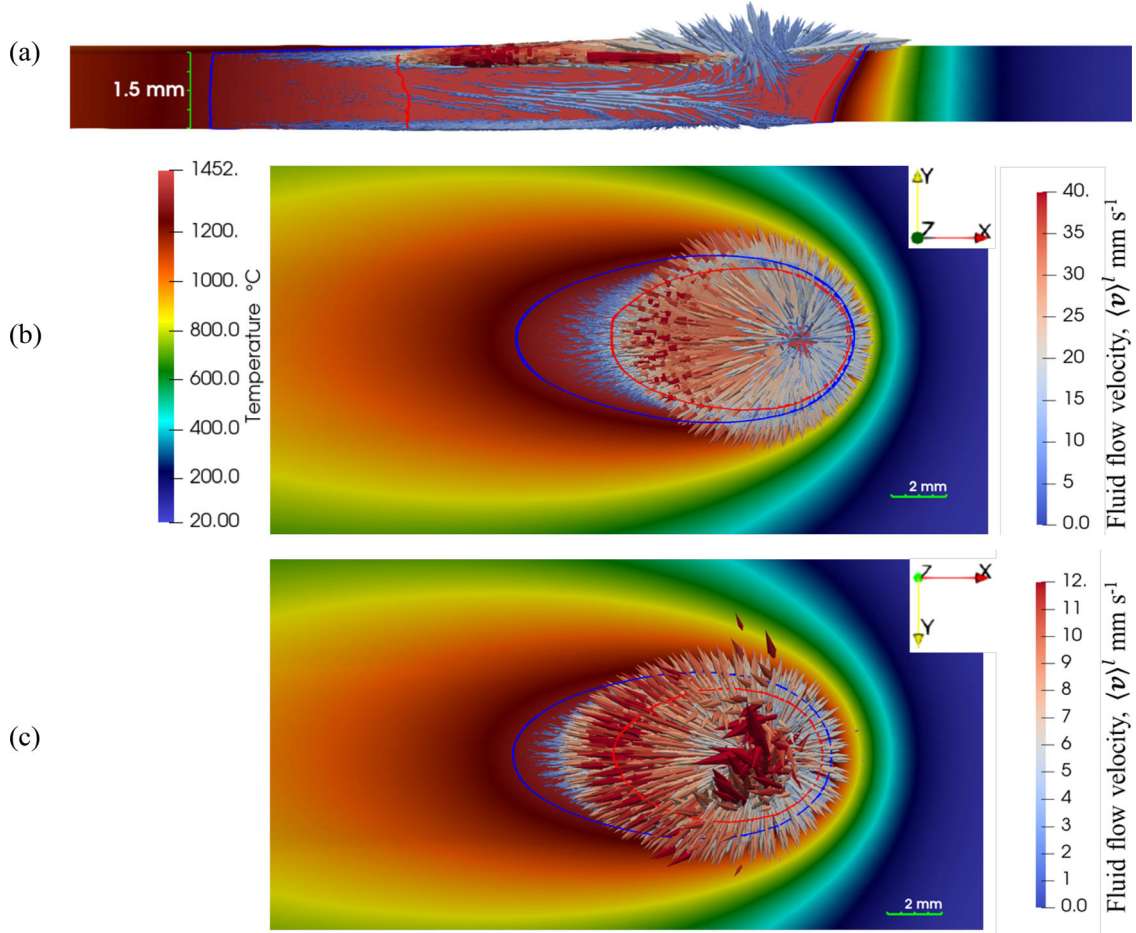### 4.1. Welding configuration V_1, kinetics law K_1, coupling scheme CO

At first, the computed temperature field and fluid flow velocity are presented in Fig. 8 for the welding configurations V_1. The air regions have been omitted to offer a better view of the metal subdomain.

Table 6
Simulation configurations.

Case	Welding velocity	Growth kinetics law	CAFE scheme	Figures
V_1K_1CO	V_1	K_1	$COupling$	8–11, 19
V_2K_1CO	V_2	K_1	$COupling$	12–15
V_1K_2CO	V_1	K_2	$COupling$	16, 17
V_1K_1CH	V_1	K_1	$CHaining$	18–20

The heat source parameters listed in Table 1 corresponds to a power $U\,I = 712$ W. However, this is not the effective power of the plasma arc, $\dot{Q}_{Plasma}$, entering equation (10). It has to be multiplied by the efficiency of the heat source, η, so as to account for the energy lost by the system, $\dot{Q}_{Plasma} = \eta\,U\,I$. This calibration is done by comparing the simulated melt pool width with measurements using the images recorded at the bottom of the plate (Fig. 3a). The value $\eta = 0.65$ was retained for the present configuration, as reported in Table 1.

The color maps in Fig. 8 gives the temperature distribution using T_L as the maximum value. The latter isotherm is also highlithed us-

Fig. 8. V_1K_1CO simulation at time 14 s. Temperature field, with (red lines) liquidus isotherm and (blue lines) solidus isotherm, and (colored arrows) liquid velocity (see Table 7) as observed (a) in the $Y = 0$ mm longitudinal cross section through the plate, as well as from (b) the top and (c) the bottom surfaces of the metallic subdomain. The gas subdomains have been omitted for clarity. The temperature scale is the same for all images and the velocity scale in (b) also applies to (a) but a different velocity scale is used in (c).

ing a red coutour. The second contour in blue gives the position of T_S. The arrows represent the direction and intensity of the liquid velocity vectors. In Fig. 8b, the top view reveals a radial outward liquid flow from a central point that corresponds to the hottest region of the melt pool located just below the heat source. The surface temperature gradient, radial and inward, creates a surface force that drives the matter towards the boundaries of the melt pool. This is typical of Marangoni-driven convection with a negative value of the $\partial\gamma/\partial T$ coefficient. The pool extends further and the liquid velocity reaches its higher value behind the heat source where the heat is preferentially transported. The flow then progressively decreases at lower temperature, which is due to the presence of solid as will be discussed later. At the lower surface of the plate, shown in Fig. 8c, a similar flow pattern is observed, with lower intensity. The velocities observed at mid-thickness ($Z = 0.75$ mm) in the longitudinal cut ($Y = 0$ mm) in Fig. 8a reveals a flow in the welding direction at the rear of the pool and in the opposite direction ahead of the heat source. So in summary, the predicted convection loops consist of two toroidal flows, one above the other, with opposite flow directions. Both toroidal flows are due to radial outward Marangoni forces created at the top and bottom liquid-gas surfaces, the top one being more intense. The maximum computed velocity at the top and bottom surfaces reaches 43 mm s^{-1} and 13 mm s^{-1}, respectively.
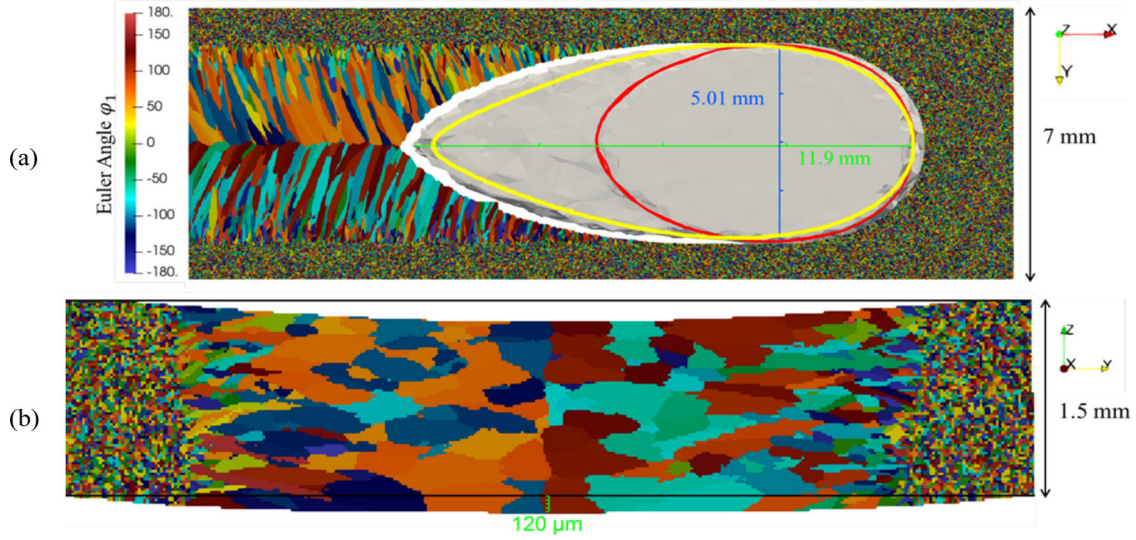
The maximum and average velocities deduced from the AVT camera viewing the lower side of the molten pool are reported in Table 7. The maximum recorded value, 34.4 mm s^{-1}, is clearly higher than in the simulation, while the average, 13.6 mm s^{-1}, is close to the maximum pre-

Table 7
Comparison between measured and simulated fields at the lower side of the plate for cases V_1K_1CO and V_2K_1CO.

Parameter			Measured	Computed	Unit
Liquid velocity	Maximum	V_1	34.4	13.2	mm s^{-1}
	Average		13.6		
	Maximum	V_2	18.5	5.9	
	Average		5.2		
Plate deflection		V_1	190	120	µm
		V_2	40	40	
Melt pool length		V_1	11.7	11.9	mm
		V_2	7.13	7.42	
Melt pool width		V_1	4.89	5.01	mm
		V_2	2.86	2.68	

dicted value. One could explain these discrepancies by the monolithic approach chosen here to solve the momentum and mass conservation equations in the whole simulation domain encompassing the gas, liquid and solid regions, with viscosities varying by several orders of magnitudes. Using realistic viscosity values lead to poor conditioning of the matrices arising when solving the momentum conservation equations, preventing a solution to be found. The pragmatic choice is then to reduce the huge gap between viscosity values. This is presently done by decreasing the apparent viscosity of the solid and increasing the viscosity of the liquid and gas phases (Table 3), leading to underestimated fluid flow. Another solution could have consisted in solving the set of

Fig. 9. V_1K_1CO simulation at time 14 s. Snapshots of (colored regions using the first Euler angle φ_1) the simulated grain structure using the CA method as observed (a) from the bottom surface and (b) in a transverse cross section after complete solidification. The melt pool shape is (grey surface) deduced from the FE simulations by considering the elements of the FE mesh with nodes such that $g_{n,FE}^l > 0.99$, (yellow contour) deduced from in-situ camera observations as already reported in Fig. 3 and (boundary between colored and white cells) identified by the growth front. The computed liquidus isotherm is added as a red contour. The total deflection of the metal-sheet plate is made visible in the transverse section by comparison with the initial planar sheet surface marked with black horizontal lines.
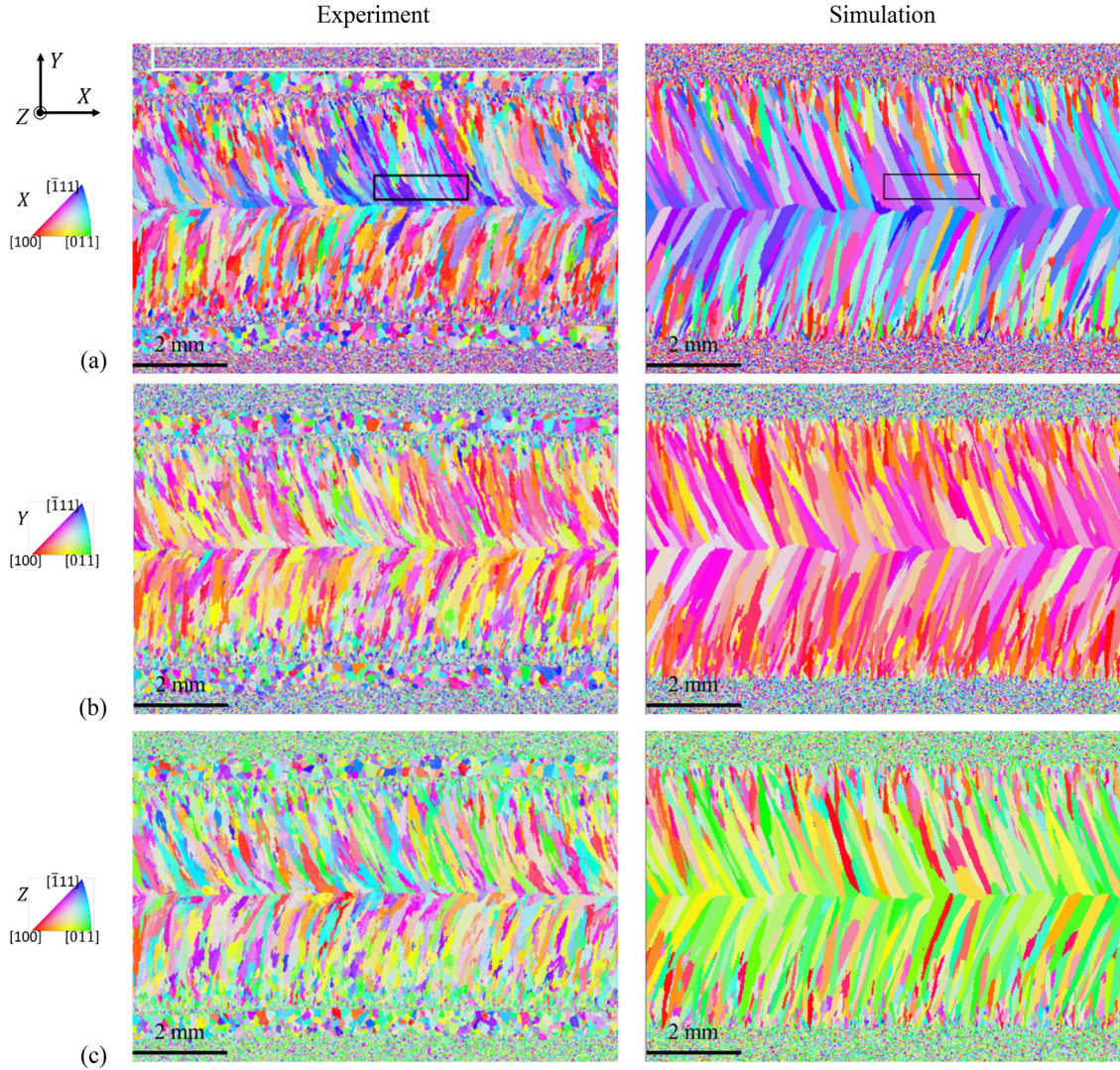
equations with momentum interactions between metallic phases modelled by the Darcy law [54,55] . With the latter approach, no viscosity value is required in the solid region so that the solution is purely fluid oriented with less variations in viscosities between the gas and liquid fluids. However, such methodology is more demanding in computing ressources and could not be conducted in the present context of welding simulations. One could also argue that maximum velocity values deduced from the PTV methodology could be overstimated due to the numerical derivation of the particle positions.

The melt pool shape seen from the bottom surface of the plate is observed by three different means in Fig. 9a. At first, the elements of the FE mesh with all nodes reaching a fraction of liquid higher than 99% are displayed in gray color. Second, the grain structure arbitrarily colored using Euler angle φ_1 is represented on the CA grid, revealing the position of the growth front with the liquid cells in white. Note that the small white gap appearing between the growth front and the fully liquid region identified in gray is a numerical artefact of the representation due to the interpolation between the FE mesh and the CA mesh and the choice of the threshold value 99% liquid to draw the molten pool. It consequently appears larger where the temperature gradient is lower, i.e. at the rear of the melt pool. Finally, the melt pool contour deduced from in-situ observations is superimposed as a yellow contour. The melt pool clearly extends further than the liquidus temperature also superimposed as a red contour. The region between the red contour and the grain structure is a metastable liquid. At the boundary of the melt pool, the dendritic grain structure either melts when the temperature exceeds T_L or grows at local temperature $T < T_L$, i.e. with local undercooling $\Delta T = T_L - T > 0$ and velocity computed according to the K_1 power law given in Table 4. Table 7 compares the length and width of the melt pool as measured and computed according to simulation V_1K_1CO, showing very good agreement. This is due to the fact that law K_1 was adjusted so as to retrieve the experimental contour. It was also verified that the melt pool dimensions are well established, i.e. they correspond to a steady regime and thus do not change with time. In fact, one can observe that the width of the images is only half the length of the CA mesh and CA grid. The heat and mass transfers as well as the computed grain structure on the left of the image displayed in Fig. 9a include transient regimes that are not considered in the comparisons with experimental results. As regard the solidification grain structure, the transverse cross section

(Fig. 9b) is not made of grains well aligned with the $\pm Y-$directions unlike what seems to be the case in the other view of the structure (Fig. 9a). In fact, a section at constant X coordinate in Fig. 9a shows that, within the weld seam, several grains are indeed encountered, thus explaining the distribution of the transverse cut. The melted and solidified width is found to be almost constant in Fig. 9b, i.e. across the whole plate thickness. This means that the teardrop shape of the melt pool in Fig. 9a is quasi two-dimensional, i.e. it is maintained along the plate thickness (Z direction). This is the result of a simple two-dimensional heat flow configuration thanks to the fully penetrated weld pool condition, that shall ease interpretation of the results. Said differently, the temperature gradient and hence the heat flow mainly lie in the plane of the plate, explaining the similar temperature fields computed at the top and bottom surfaces of the plate shown in Fig. 8.

Simulations also include the plate subsidence with maximum deflection located at the center of the weld seam. Fig. 9b shows the result as observed after it was transferred to the CA mesh and used by the CA grid to compute the grain structure. The computed value, 120 µm, is to be compared to the measurement reported in Table 7, reaching 190 µm. As discussed before, underestimation could be linked to the monolithic solver using too large viscosity, thus underestimating the flow intensity.

Quantitative comparison is also done for the grain structure and texture in Fig. 10. The representation is complementary to the structure displayed in Fig. 9 where the colors were only used to distinguish between grains, with no possibility to interpret it as a texture. Only a small part of the simulation domain is displayed in the right-hand-side images of Fig. 10, that corresponds to the same dimensions as the scanned surfaces using EBSD displayed in the left-hand-side images. Three inverse pole figures (IPF) are made available, that correspond to the orientation of the grains projected along the (a) $X-$, (b) $Y-$ and (c) $Z-$ directions. The three images permit a full representation of the crystallography of the grains. One first observation is that the grain size in the base plate, far from the heat affected zone, is very fine and well represented by the simulation. For that, the cell size was indeed chosen smaller than the initial grain size and the measured grain density was used to generate the base plate grain structure. In Fig. 10, focusing on the base metal, one can notice that the IPF-X, IPF-Y and IPF-Z color maps are different but the experimental and simulated maps are similar. This is due to the initialization procedure of the grain structure. The orientation of
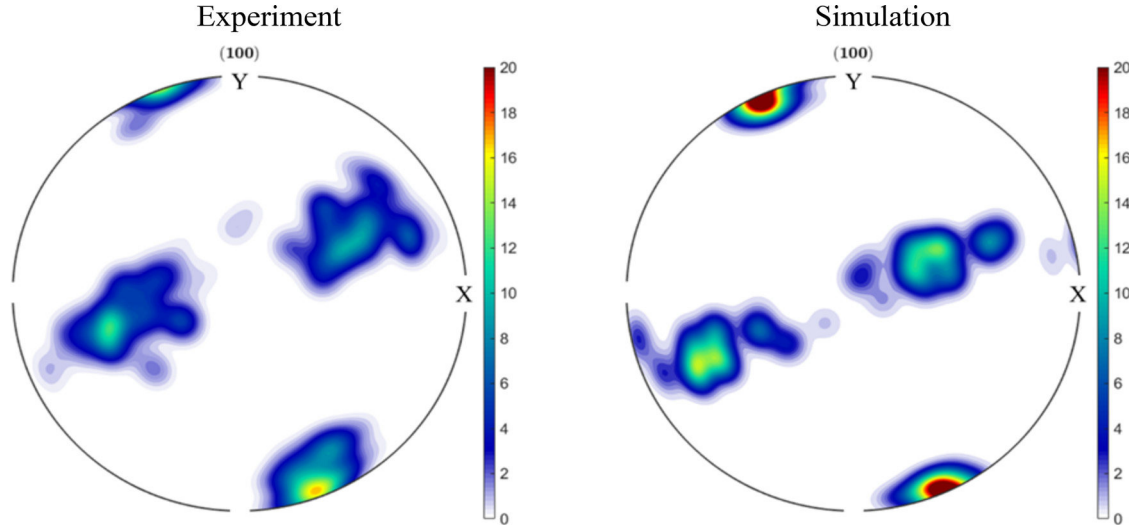
Fig. 10. $V_1 K_1 CO$ simulation. EBSD maps of the grain structure in a $Z-$ plane close to the bottom surface (left) measured and (right) simulated with the CAFE model. The inverse pole figure color codes used are with respect to the (a) $X-$, (b) $Y-$ and (c) $Z-$ directions.

all the grains located in the white window highlighted in the measured EBSD data (Fig. 10a) is stored as representative of the base metal texture. Upon generation of the simulated grain structure of the base metal, the orientation of each new grain is randomly chosen among the stored data, hence reproducing the initial texture. It should be added that a random selection of the grain orientation was also tried, that led to similar color distributions for all EBSD IPF maps, thus not reproducing well the initial texture of the base plate.

Overall, an elongated solidification grain structure is observed, typical of columnar growth, with a center line marked around $Y = 0$ mm. This observation explains the choice made here to model no nucleation in the melt pool. The overall colors of the grains are also compared, starting with the IPF-Y maps (Fig. 10b). A mixture of red, orange, pink and yellow colors is found close the weld seam boundaries, that turn to a dominance of pink towards the centerline. These grains have one of their $\langle 100 \rangle$ directions misaligned with the $Y-$direction by around 25°, corresponding to the orientation of the temperature gradient close to the seam boundaries displayed in Fig. 9a, hence explaining the selection of those grains. As a consequence, all grains in blue and green in Fig. 10b do not survive the grain growth competition. Going from the boundaries to the centerline of the weld seam, Fig. 9a shows that the normal to the growth front (or melt pool boundary) progressively turns toward the $\pm X-$direction up to around 25° This explains the elimination

of the red grains in Fig. 10b (with well aligned $\langle 100 \rangle$ direction along the $\pm Y-$directions) at the centerline of the weld, and subsistence of only the pink grains. However, more colors remain at the centerline of the experimental EBSD IPF-Y map (Fig. 10b left), not present in the simulation. One could argue that, even if the trend of grain selection is well reproduced by the model, it occurs faster compared to the measurement when going from the boundaries to the centerline of the weld seam. The grain density is also slightly higher in the measurements. These differences could be the results of a small source of new grains formed by either nucleation or fragmentation in the undercooled liquid, that contribute to growth competition with the grains coming from the initial plate structure. This source of additional grains has not been added to the simulations.

The simulated grain structures drawn for IPF-X and IPF-Z maps also compare favorably. This means that the CA growth algorithm indeed correctly selects the crystal directions that are complementary to the main selection mechanism of the $\langle 100 \rangle$ directions with the temperature gradient at the growth front. A more quantitative information is given in Fig. 11. The $\langle 100 \rangle$ pole figures of the grains located in the black rectangle drawn in Fig. 10a are plotted from (left) the recorded and (right) the simulated orientation maps. The windows are chosen close to the center of the weld (small Y value) in the $+Y$ mid-plane where the temperature gradient at the growth front takes positive X and negative Y

Fig. 11. $V_1 K_1 CO$ simulation. $\langle 100 \rangle$ pole figure of the grain structure located in the black rectangle in Fig. 10 (left) measured and (right) simulated with the CAFE model.

components. A strong fiber texture is revealed that coincides with selected grains having a $\langle 100 \rangle$ direction along the corresponding direction of the temperature gradient at the growth front, explaining the deviation from the Y-direction by around 25° The magnitude of the fiber texture is revealed by the color in Fig. 11. It is higher in the predicted grain structure, in agreement with the observations of the lower grain density and less variations of the colors in the black windows compared to the measurements. One can also see that the distribution other $\langle 100 \rangle$ directions are more or less distributed along a line going through the center of the pole figures, with a 25° misorientation with respect to the X-direction. They correspond to the secondary $\langle 100 \rangle$ growth directions of the microstructures, i.e. to branches of the dendritic structure more or less perpendicular to the temperature gradient and to the fiber texture. It was verified that a random crystal orientation of the initial grain structure (i.e., not based on the sampling taken from the grain structure located in the white window in Fig. 10a and thus not reproducing the initial grain texture of the base metal) leads to a more uniformly distributed secondary orientation along the 25° line. One can also notice that the distribution of the secondary $\langle 100 \rangle$ directions in Fig. 11 corresponds to a $\langle 110 \rangle$ fiber texture in the Z-direction, explaining the dominance of green colors in Fig. 10c. Besides, a grain coarsening phenomenon is experimentally observed at the border of the melt pool in the heat affected zone as also reported in the literature [56,57]. This is also not considered in the present simulations.

4.2. Welding configuration V_2, kinetics law K_1, coupling scheme CO

Configuration $V_2 K_1 CO$ proposes a different welding speed, $V_2 = 4.3$ mm s^{-1}. The effective power of the plasma arc is almost similar, with $\dot{Q}_{Plasma} = \eta\, U\, I = 463$ W for case $V_1 K_1 CO$ and $\dot{Q}_{Plasma} = 424$ W for case $V_2 K_1 CO$ (Table 1). As a consequence, the linear energy $\dot{Q}_{Plasma}/V$ is decreased and a smaller melt pool is expected. Fig. 12 clearly shows this trend. A similar superposition of two toroidal flows is simulated, with a decreased intensity of the maximum liquid velocity. Table 7 again gathers information for comparison with measurements. As for the previous case, the maximum computed liquid velocity, 5.9 mm s^{-1}, is close to the average measurement, 5.2 mm s^{-1}.

Fig. 13a again shows the shape and dimensions of the melt pool to be compared with measurement (Fig. 3b, Table 7). The length and width of the met pool, 7.42 mm and 2.68 mm, but also the maximum computed deflection shown in Fig. 13b, 40 μm, retrieves very well the measured values. The latter reflects a smaller subsidence expected for a smaller pool that solidifies faster. Considering that no simulation parameter is

changed compared to $V_1 K_1 CO$ but the welding velocity, these results are very consistent. The EBSD map in Fig. 14 is only shown for IPF-X. The same observations as for Fig. 10 can be made. The grain size measured is smaller as the melt pool width is smaller. This is also found by the simulation as the grains have less distance to compete prior to meeting at the centerline. Another consequence is a less texture and oriented grain structure compared to the lower velocity case $V_1 K_1 CO$. This is quantitatively shown in Fig. 15 where the $\langle 100 \rangle$ pole figure is drawn, corresponding to the grains falling in the rectangle window displayed in Fig. 14. The fiber texture is retrieved in the direction of the temperature gradient at the growth front, with a positive X and negative Y components as for the reference case $V_1 K_1 CO$. However, the intensity of the texture is weaker as revealed by comparing the colors in the experimental data drawn in Fig. 11 (intensity = 17) and Fig. 15 (intensity = 16). The same trend is found when comparing Fig. 11b and Fig. 15b. The $\langle 100 \rangle$ pole figure for the V_2 experiment also show that the texture as a small Z component, not fully retrieved by the simulation.

5. Discussion

As stated in section 4.1, the efficiency of the heat source was first calibrated by comparing the width of the melt pool rather than its length. The reason for this choice is that the growth front at maximum width corresponds to the transition region between remelting and solidification. It should therefore be independent on the growth kinetics law as the local front undercooling tends toward zero at this particular location. So even if the calibration was carried out using simulations $V_1 K_1 CO$ and $V_2 K_1 CO$, a similar melt pool width is expected when using whatever kinetics law that cancels the velocity at no undercooling. However, the length of the melt pool was clearly retrieved by adjusting the coefficients of the growth kinetics, K_1. And the fact that the same growth law gives good melt pool length for the two welding velocities is again encouraging. Hereafter we question the validity of using a computed dendrite tip growth kinetics in the simulation $V_1 K_2 CO$. Then the practice of chaining rather than coupling is illustrated in simulation $V_1 K_1 CH$. For these two simulations, case $V_1 K_1 CO$ serves as the reference.

5.1. Welding configuration V_1, kinetics law K_2, coupling scheme, CO

The growth law K_2 reported in Table 4 was deduced from PhysalurgY [34], a library of physical metallurgy modules coupled with Thermo-Calc [58]. One of the modules is based on the multicomponent dendrite tip kinetic model developed by Hunziker [48] using with the TCFE9
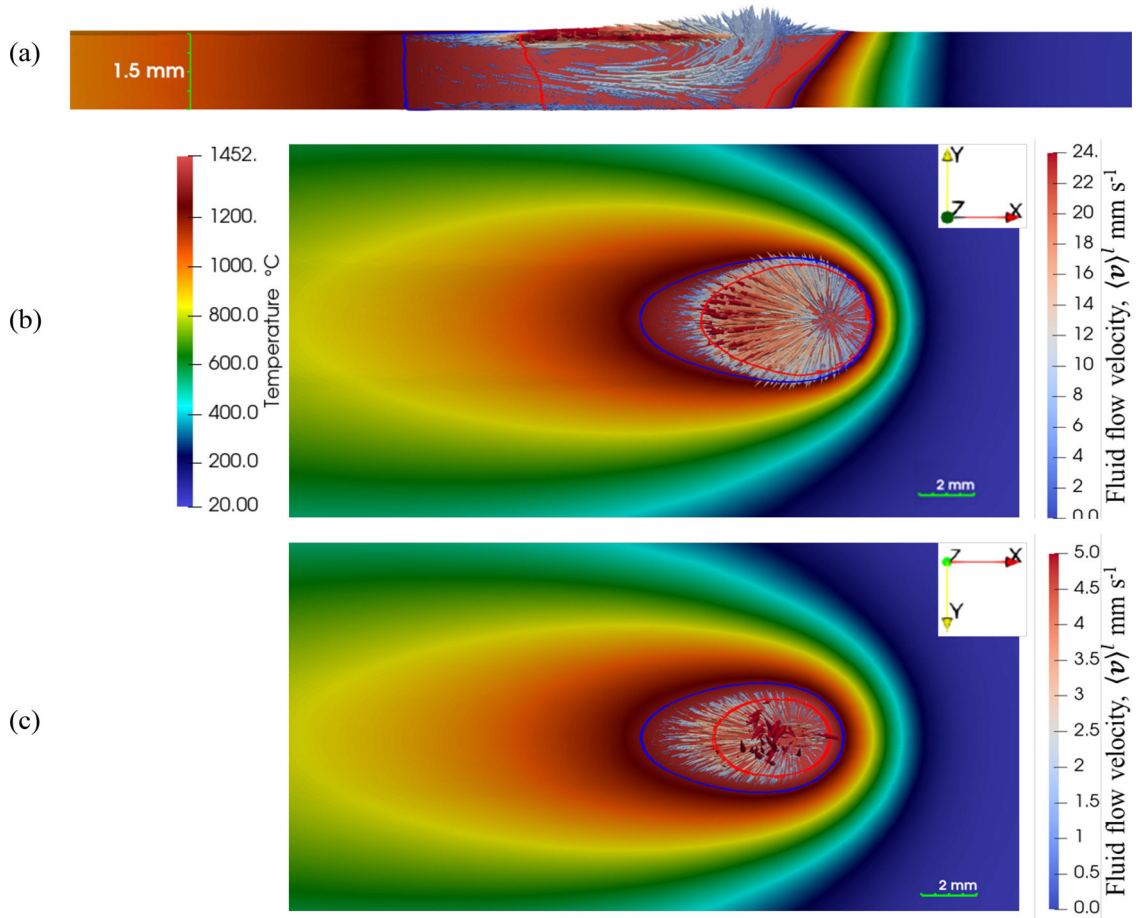
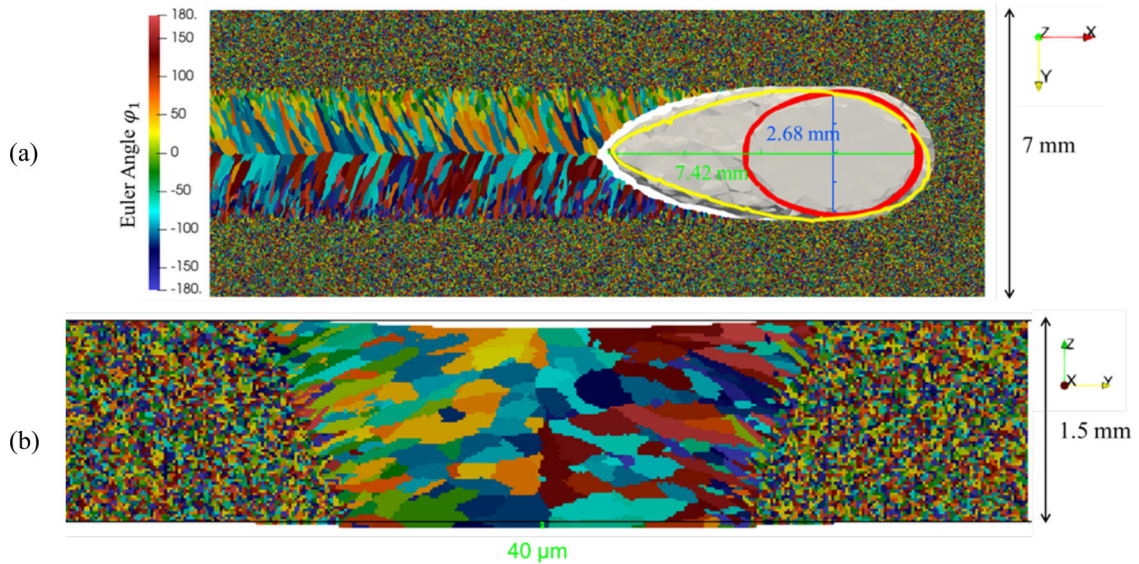**Fig. 12.** V_2K_1CO simulation at time 14 s. Same as Fig. 8 caption.

Fig. 13. V_2K_1CO simulation at time 14 s. Same as Fig. 9 caption.

database [30] to access thermodynamic equilibrium assumed at the solid/liquid interface and the MOBFE6 database to compute diffusion data in the liquid phase [59]. Reading the two mathematical expressions of the growth kinetics law in Table 4, one can immediately realize that, at a given velocity, a very small undercooling is computed with K_2 compared to K_1.

As in Fig. 9 and Fig. 13, the region of undercooled liquid computed in case V_1K_2CO reported in Fig. 16 lies between the growing front delimited by the grains/liquid boundary and the T_L (red contour). It could be noted that two contours can be observed, due to the 3D presentation of T_L contours mixed at different thickness at the end of the melt pool. As expected, the undercooled region is significantly reduced when using
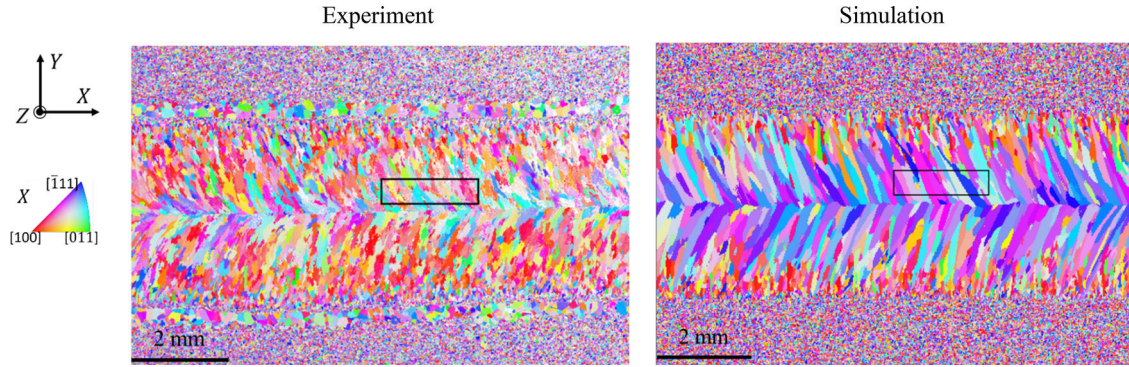
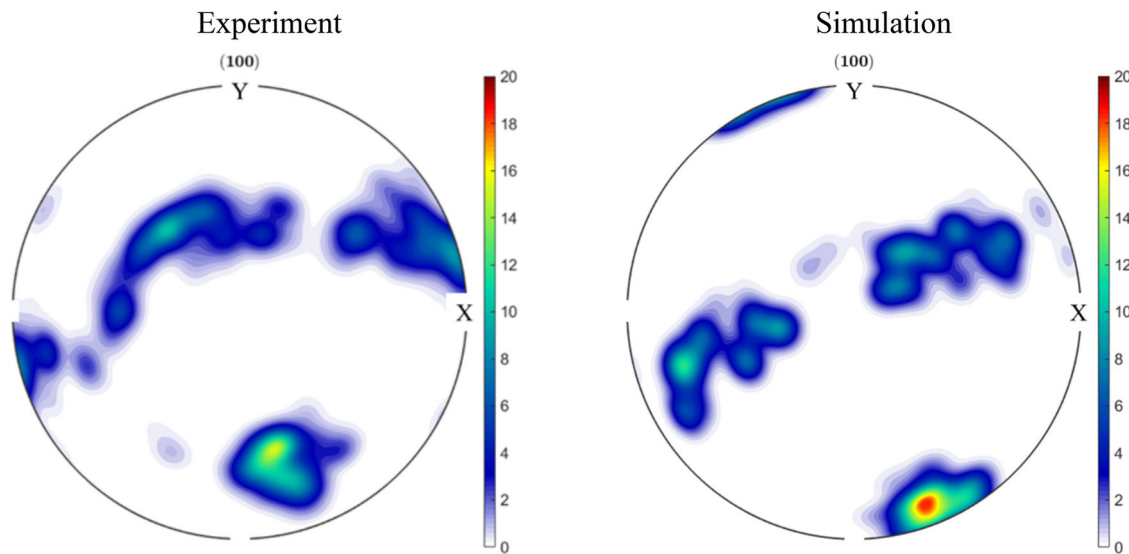**Fig. 14.** V_2K_1CO simulation. Same as Fig. 10 caption.

Fig. 15. V_2K_1CO simulation. $\langle 100 \rangle$ pole figure of the grain structure located in the black rectangle in Fig. 14 (left) measured and (right) simulated with the CAFE model.
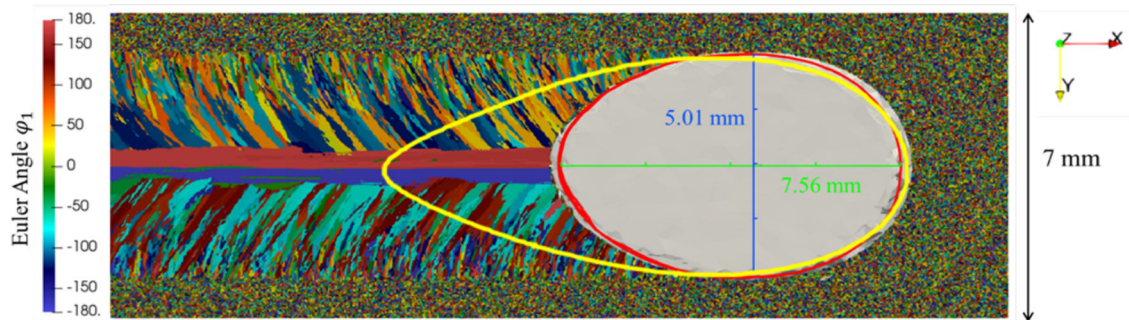

Fig. 16. V_1K_2CO simulation at time 14 s. Same as Fig. 9a caption.

the K_2 kinetics law compared to its dimension computed in Fig. 9 with the K_1 kinetics law and the same welding velocity V_1. As a consequence, the melt pool shape (region coloured in gray) does no longer represent well the experimental observation (yellow contour). A spectacular consequence is the predicted grain structure. Because the growth front is close to T_L, it adopts a rounder shape and the temperature gradient at the growth front more progressively evolves from the $\pm Y$-directions at maximum width to the $+X$-direction at the centerline of the weld seam. As a consequence, grain competition is less directional compared to the reference case V_1K_1CO and some grains with a $\langle 100 \rangle$ direction aligned with the $+X$-direction survive the competition and remain present at the centerline of the weld seam. Fig. 17 confirms this interpretation.

The simulated IPF-X map shows that hot colors for the grains at the centerline and almost all colors are represented in the columnar grain structure. Compared to the experimental EBSD map (Fig. 10a), the result is clearly not as close as the simulated map using the K_1 kinetics law (Fig. 10b). This result shows the importance of the representation of the melt pool, which in turns required a satisfying growth kinetics law.

The relevance of a computed dendrite tip kinetics is then to be discussed. Despite the use of the most recent databases [30,59], several material parameters of the model are doubtful. They include the diffusion matrix and the ferrite-liquid interfacial energy, as well as the stability constant taken equal to $(2\pi)^{-2}$ [49]. But more questionable are
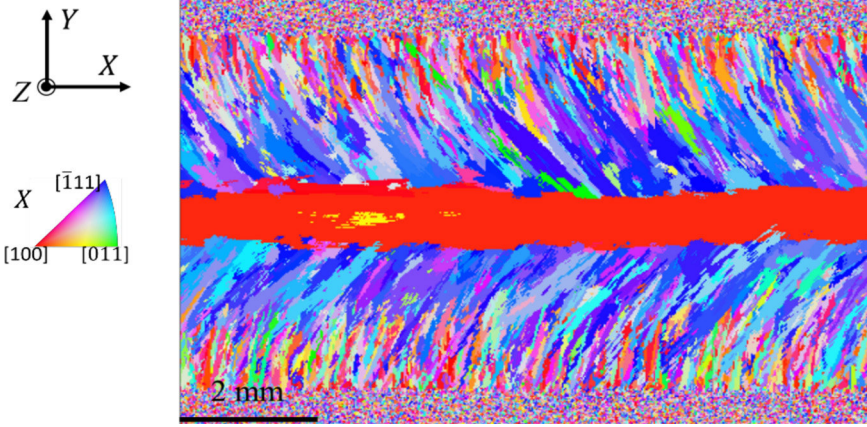
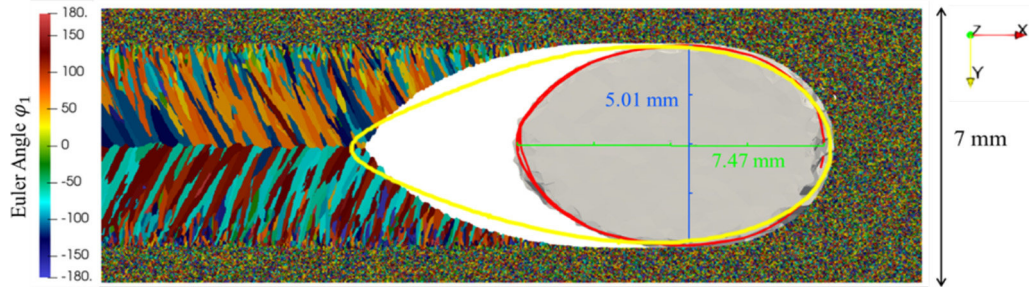Fig. 17. V_1K_2CO simulation. Same as Fig. 10a caption.

Fig. 18. V_1K_1CH simulation at time 14 s . Same as Fig. 9a caption.

the assumptions of the model that consider no rapid solidification effect. These are solute trapping and kinetics undercooling [50]. Solute trapping is explained by the difficulty of liquid atoms to attach to the solidifying interface while maintaining thermodynamic equilibrium. Kinetics undercooling is linked to the kinetics of attachment of the atoms to the solidifying interface. These contributions are expected to have an influence at high velocity, increasing the solubility of the solid phase as well as the total undercooling of the growth front. The present simulation results suggest that more efforts should be concentrated on the validation of the dendrite growth kinetics at high velocity.

Finally, while in-situ observations of the melt pool bring invaluable information, it is regretful that no measurement of the temperature fields was made possible with the present experimental configuration. The main validation of the heat flow is based on the width of the melt pool supposed to correspond to the limits given by the liquidus isotherm. But the use of an infrared camera and well-located thermocouple would have also been very useful. In fact, the computed temperature field suggests that the growth undercooling overpasses 150°C and is thus of the order of the solidification interval. This again is in favor of high velocity effects that would add on a kinetic contribution to the total undercooling. Yet this could have been validated with temperature measurements, that were not available in the present experiments.

5.2. Welding configuration V_1, kinetics law K_1, chaining scheme CH

The chaining scheme of the CAFE model is now tested. This is done by comparing the V_1K_1CH simulation against the corresponding V_1K_1CO reference case using the coupling scheme. It is worth saying that most if not all direct grain structure simulations in the literature are based on the chaining scheme as it is the simplest to operate.

As detailed in chapter 3.5, with the chaining scheme, the conversion of energy into a temperature makes use of the tabulated phase enthalpies and phase fractions listed in Fig. 2 whatever the grain structure is. The resulting temperature field is then uniquely defined. It serves to compute the grain structure after its transfer to the CA mesh and the CA
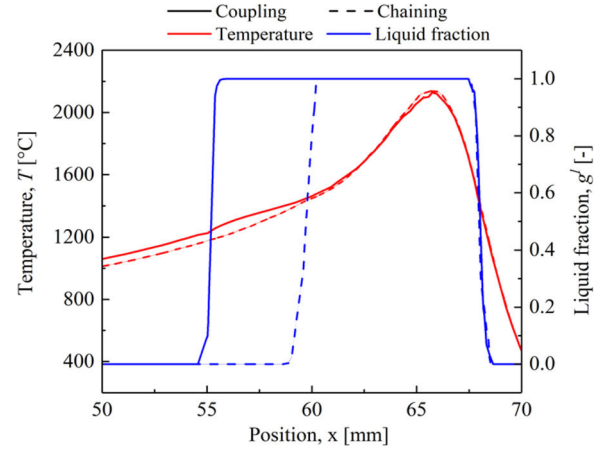

Fig. 19. Comparison of profiles at time 14 s for (red) the temperature and (blue) the liquid fraction as observed along the centerline ($X-$ line) draw at the center of the melt pool ($Y = 0$ mm) at depth $Z = 0.75$ mm, with (plain lines) the coupling scheme, V_1K_1CO, and (dashed lines) the chaining scheme, V_1K_1CH.

grid schematized in Fig. 6. The predictions using the chaining scheme are presented in Fig. 18 to Fig. 20 and Fig. 19. When drawing the melt pool defined by more than 99% liquid fraction, it is naturally limited to the superheated liquid region and hence encompassed within the T_L isotherm contour (in red in Fig. 18). The same result is show when drawing the profiles of temperature and liquid fraction along the centerline of the weld seam in Fig. 19. The chaining scheme results show that the liquid fraction simply follows the tabulations in Fig. 2, decreasing below T_L and reaching 0% below T_S. This position clearly differs from the growth front of the grain structure predicted by the CA method using K_1 in Fig. 18. It is indeed located ways behind the melt pool predicted by the solution of the conservation equations. For this reason, a large region
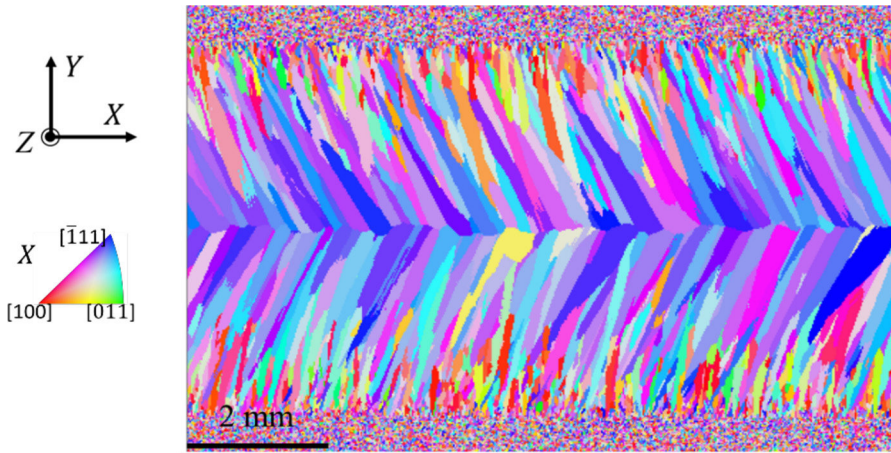
Fig. 20. $V_1 K_1 CH$ simulation. Same as Fig. 10a caption.

appears behind the melt pool predicted by the conservation equations (in gray), that correspond to CA cells with an index still corresponding to the liquid state (in white). This can be seen as an inconsistent result between the CA and FE solutions due to the chaining scheme, that was not present in Fig. 9a with the coupling scheme: the CA grain structure computed by chaining actually develops in a region where solid is already formed according to the FE solution. Comparison of the profiles for the chaining and coupling schemes is possible in Fig. 19, also confirming this the consistent behavior between CA and FE fields by the coupling scheme where the existence of a mushy zone (non-liquid cells), $g_{v,CA}^m$, is used to convert energy into fraction of phases and hence resulting into slightly different temperature field (Fig. 6).

One should now consider the consequences of the chaining scheme on the grain structure. While similitudes exist between the computed grain structures in Fig. 18 and Fig. 9a, the growth front is not as sharp at the rear of the melt pool when using chaining. As a consequence, a small difference exists in the average grain orientation, of the order of 10° more inclined in Fig. 18. This is also seen when comparing Fig. 20 with Fig. 10a showing the EBSD IPF-X maps. More dark blue colors are found in Fig. 20; confirming the increased inclination of the grains. Thus, the chaining scheme has less consequences on the grain structure compared to the growth kinetics law. The main reason is due to the high temperature gradient and the constrained growth mode that drives energy through the surrounding cold metal plate. In case of lower temperature gradient processing, e.g. casting of thick metal component, the development of the grain structure acts more significantly on the overall temperature field. The most obvious example is the formation of an equiaxed grain structure for which recalescence events are regularly reported [10,52].

It is also worth noticing that the chaining scheme could have been used to determine the adjusted growth law, K_1, while this was presently done using coupling in simulation $V_1 K_1 CO$. This would have obviously required to compare the shape of the CA computed growth front with the observed melt pool boundary and not the FE computed melt pool (see Fig. 18). However, this strategy was not pursued as it presents inconsistent as previously discussed.

6. Conclusions and perspectives

Thanks to in-situ observations and EBSD measurements on dedicated GTAW welding experiments of thin metal-sheet plates, quantitative comparisons with melt pool shape, subsidence and grain structure simulations have been carried out. The main findings are summarized hereafter.

- A monolithic FE formulation accounting for the metal and gas subdomains with a free moving LS boundary between subdomains is able to give solutions for heat and fluid flows as well as to predict the subsidence due to the fully penetrated welding configuration.
- The overall grain structure and its associated texture can well be reproduced by the CA method providing a satisfying shape of the melt pool is predicted. The latter melt pool shape is directly dependent on the growth undercooling at the melt pool boundary with the growing grain structure, requiring an adjustment of the growth kinetics law. A unique such law can retrieve the melt pool shape and the grain structure for two welding velocities.
- A computed dendrite tip growth kinetics [34,48] using thermodynamic databases [30,59] for interface equilibrium and diffusion coefficients does not succeed in predicting the melt pool shape. Rapid solidification phenomena, not included in the growth kinetics model, may be at the origin of this discrepancy.
- The limitations of the chaining scheme compared to the coupling scheme of the CAFE model are highlighted.

Several directions are suggested for future investigations and improvements of the CAFE model applied to welding processes:

- The growth kinetics law, of prime importance for quantitative prediction of the grain structure, must include rapid solidification phenomena and comparison with dedicated experiments.
- Fluid mechanics solvers including permeability of the mushy zone to progressively reduce the velocity to zero in the solid region should be favored in order to use nominal fluid properties in both the air and the liquid phases, although it may require more computational resources. Coupling with a partitioned two-step solution algorithm for concurrent fluid flow and stress-strain predictions [55] is yet expected to be the method of choice for improvement of the plate subsidence.
- Grains coarsening taking place in the heat affected zone is not modelled by the present CAFE model that only consider the fusion zone where melting and solidification takes place. Such effect is accounted for in the literature and could be added to the present model.
- The virtual grain structure computed by CAFE simulations should be used for software dedicated to compute non-destructive test (NDT) in welds, e.g. by computing ultrasound propagation that are very dependent on the metallurgical state of the mater. This is expected to improve prediction and enhance reliability of the NDT modeling software.
- The virtual solidifying grain structure could be used for improvement of thermomechanical simulations and hot tearing criteria as this defect is known to highly depend on the distribution of grain boundaries.

Declaration of Competing Interest

The authors declare that they have no known competing financial interests or personal relationships that could have appeared to influence the work reported in this paper.

Acknowledgments

References

[1] M.I. Khan, Welding science and technology, New Age International (2007).

[2] M. Rappaz, J.A. Dantzig, Solidification (2009).

[3] S.K. Banerji, C.L. Briant, Embrittlement, engineering alloys, in: R.A. Meyers (Ed.), Encycl. Phys. Sci. Technol., Third Ed., Academic Press, New York, 2003, pp. 407–432, doi:10.1016/B0-12-227410-5/00221-0.

[4] T.-.L. Teng, C.-.C. Lin, Effect of welding conditions on residual stresses due to butt welds, Int. J. Press. Vessels Pip. 75 (1998) 857–864, doi:10.1016/S0308-0161(98)00084-2.

[5] R. Pierer, C. Bernhard, C. Chimani, A contribution to hot tearing in the continuous casting process, Rev. Métallurgie–International J. Metall. 104 (2007) 72–83.

[6] N. Wang, S. Mokadem, M. Rappaz, W. Kurz, Solidification cracking of superalloy single- and bi-crystals, Acta Mater 52 (2004) 3173–3182, doi:10.1016/j.actamat.2004.03.047.

[7] F. Yusof, M.F. Jamaluddin, 6.07 - Welding Defects and Implications on Welded Assemblies, in: S. Hashmi, G.F. Batalha, C.J. Van Tyne, B. Yilbas (Eds.), Compr. Mater. Process, Elsevier, Oxford, 2014, pp. 125–134, doi:10.1016/B978-0-08-096532-1.00605-1.

[8] P.E. Lhuillier, B. Chassignole, M. Oudaa, S.O. Kerhervé, F. Rupin, T. Fouquet, Investigation of the ultrasonic attenuation in anisotropic weld materials with finite element modeling and grain-scale material description, Ultrasonics 78 (2017) 40–50, doi:10.1016/j.ultras.2017.03.004.

[9] M. Rappaz, Ch.-A. Gandin, Probabilistic modelling of microstructure formation in solidification processes, Acta Metall. Mater. 41 (1993) 345–360, doi:10.1016/0956-7151(93)90065-Z.

[10] Ch.-A. Gandin, M. Rappaz, A coupled finite element-cellular automaton model for the prediction of dendritic grain structures in solidification processes, Acta Metall. Mater. 42 (1994) 2233–2246, doi:10.1016/0956-7151(94)90302-6.

[11] M. Rappaz, C.A. Gandin, J.-.L. Desbiolles, P. Thevoz, Prediction of grain structures in various solidification processes, Metall. Mater. Trans. A. 27 (1996) 695–705.

[12] S.-.M. Seo, I.-.S. Kim, C.-.Y. Jo, K. Ogi, Grain structure prediction of Ni-base superalloy castings using the cellular automaton-finite element method, Mater. Sci. Eng. A. 449–451 (2007) 713–716, doi:10.1016/j.msea.2006.02.400.

[13] C.-.A. Gandin, J.-.L. Desbiolles, M. Rappaz, P. Thevoz, A three-dimensional cellular automation-finite element model for the prediction of solidification grain structures, Metall. Mater. Trans. A. 30 (1999) 3153–3165.

[14] S. Chen, G. Guillemot, C.-.A. Gandin, 3D coupled cellular automaton (ca)-finite element (fe) modeling for solidification grain structures in gas tungsten arc welding (GTAW), ISIJ Int 54 (2014) 401–407, doi:10.2355/isijinternational.54.401.

[15] S. Chen, G. Guillemot, C.-.A. Gandin, Three-dimensional cellular automaton-finite element modeling of solidification grain structures for arc-welding processes, Acta Mater 115 (2016) 448–467, doi:10.1016/j.actamat.2016.05.011.

[16] A. Chiocca, F. Soulié, F. Deschaux-Beaume, C. Bordreuil, Study of the effect of growth kinetic and nucleation law on grain structure simulation during gas tungsten arc welding of Cu-Ni plate, Weld. World. 63 (2019) 887–901, doi:10.1007/s40194-019-00717-0.

[17] R. Han, W. Dong, S. Lu, D. Li, Y. Li, Modeling of morphological evolution of columnar dendritic grains in the molten pool of gas tungsten arc welding, Comput. Mater. Sci. 95 (2014) 351–361, doi:10.1016/j.commatsci.2014.07.052.

[18] R. Han, S. Lu, W. Dong, D. Li, Y. Li, The morphological evolution of the axial structure and the curved columnar grain in the weld, J. Cryst. Growth. 431 (2015) 49–59, doi:10.1016/j.jcrysgro.2015.09.001.

[19] L. Chen, Y. Wei, S. Qiu, W. Zhao, Macro–micro scale modeling and simulation of columnar grain evolution during gas tungsten arc welding of nickel-based alloy GH3039, Metall. Mater. Trans. A. 51 (2020) 887–896, doi:10.1007/s11661-019-05546-w.

[20] J.A. Koepf, D. Soldner, M. Ramsperger, J. Mergheim, M. Markl, C. Körner, Numerical microstructure prediction by a coupled finite element cellular automaton model for selective electron beam melting, Comput. Mater. Sci. 162 (2019) 148–155, doi:10.1016/j.commatsci.2019.03.004.

[21] J. Zhang, F. Liou, W. Seufzer, K. Taminger, A coupled finite element cellular automaton model to predict thermal history and grain morphology of Ti-6Al-4 V during direct metal deposition (DMD), Addit. Manuf. 11 (2016) 32–39, doi:10.1016/j.addma.2016.04.004.

[22] Y. Zhang, J. Zhang, Modeling of solidification microstructure evolution in laser powder bed fusion fabricated 316 L stainless steel using combined computational fluid dynamics and cellular automata, Addit. Manuf. 28 (2019) 750–765, doi:10.1016/j.addma.2019.06.024.

[23] K. Teferra, D.J. Rowenhorst, Optimizing the cellular automata finite element model for additive manufacturing to simulate large microstructures, Acta Mater 213 (2021) 116930, doi:10.1016/j.actamat.2021.116930.

[24] F. Xiong, C. Huang, O.L. Kafka, Y. Lian, W. Yan, M. Chen, D. Fang, Grain growth prediction in selective electron beam melting of Ti-6Al-4 V with a cellular automaton method, Mater. Des. 199 (2021) 109410, doi:10.1016/j.matdes.2020.109410.

[25] C.A. Gandin, M. Rappaz, D. West, B.L. Adams, Grain texture evolution during the columnar growth of dendritic alloys, Metall. Mater. Trans. A. 26 (1995) 1543–1551.

[26] A. Pineau, G. Guillemot, D. Tourret, A. Karma, Ch.-A. Gandin, Growth competition between columnar dendritic grains – Cellular automaton versus phase field modeling, Acta Mater 155 (2018) 286–301, doi:10.1016/j.actamat.2018.05.032.

[27] E. Dorari, K. Ji, G. Guillemot, C.-.A. Gandin, A. Karma, Growth competition between columnar dendritic grains – The role of microstructural length scales, Acta Mater 223 (2022) 117395, doi:10.1016/j.actamat.2021.117395.

[28] N. Blanc, F. Soulié, I. Bendaoud, S. Rouquette, F. Deschaux-Beaume, C. Bordreuil, Fluid flow measurements in fully penetrated 316 L TIG welding, Sci. Technol. Weld. Join. (2021) n.d.

[29] EN10088-4, Stainless steels - Technical delivery conditions for sheet/plate and strip of corrosion resisting steels for construction purposes, (2009).

[30] Steel and Fe-Alloys – TCFE, Thermo-Calc Softw. (n.d.). https://thermocalc.com/products/databases/steel-and-fe-alloys/ (accessed July 12, 2021).

[31] T. Koshikawa, C.-.A. Gandin, M. Bellet, H. Yamamura, M. Bobadilla, Computation of phase transformation paths in steels by a combination of the partial-and para-equilibrium thermodynamic approximations, ISIJ Int 54 (2014) 1274–1282.

[32] X. Li, F. Gao, J. Jiao, G. Cao, Y. Wang, Z. Liu, Influences of cooling rates on delta ferrite of nuclear power 316H austenitic stainless steel, Mater. Charact. 174 (2021) 111029, doi:10.1016/j.matchar.2021.111029.

[33] J.W. Elmer, J. Wong, T. Ressler, In-situ observations of phase transformations during solidification and cooling of austenitic stainless steel welds using time-resolved x-ray diffraction, Scr. Mater. 43 (2000) 751–757, doi:10.1016/S1359-6462(00)00481-4.

[34] G. Guillemot, https://physalurgy.cemef.mines-paristech.fr/, (n.d.). https://physalurgy.cemef.mines-paristech.fr/(accessed July 12, 2021).

[35] O. Muránsky, M.C. Smith, P.J. Bendeich, L. Edwards, Validated numerical analysis of residual stresses in Safety Relief Valve (SRV) nozzle mock-ups, Comput. Mater. Sci. 50 (2011) 2203–2215, doi:10.1016/j.commatsci.2011.02.031.

[36] D.B. Allan, T. Caswell, N.C. Keim, C.M. van der Wel, R.W. Verweij, soft-matter/trackpy: trackpy v0.5.0, Zenodo (2021), doi:10.5281/zenodo.4682814.

[37] J.U. Brackbill, D.B. Kothe, C. Zemach, A continuum method for modeling surface tension, J. Comput. Phys. 100 (1992) 335–354, doi:10.1016/0021-9991(92)90240-Y.

[38] M. Shakoor, B. Scholtes, P.-.O. Bouchard, M. Bernacki, An efficient and parallel level set reinitialization method – Application to micromechanics and microstructural evolutions, Appl. Math. Model. 39 (2015) 7291–7302, doi:10.1016/j.apm.2015.03.014.

[39] M. Rappaz, M. Bellet, M. Deville, Numerical Modeling in Materials Science and Engineering, Springer Science & Business Media, 2010.

[40] A. Saad, Modélisation par level set des macroségrégations induites par le retrait à la solidification, These de doctorat, Paris Sciences et Lettres (ComUE) (2016) http://www.theses.fr/2016PSLEM026. (accessed August 10, 2021).

[41] S. Zhang, Numerical simulation of mechanical interactions between liquid and solid phase in solidification processes thesis, Université Paris sciences et lettres, 2020.

[42] O. Desmaison, M. Bellet, G. Guillemot, A level set approach for the simulation of the multipass hybrid laser/GMA welding process, Comput. Mater. Sci. 91 (2014) 240–250, doi:10.1016/j.commatsci.2014.04.036.

[43] A. Saad, C.-.A. Gandin, M. Bellet, Temperature-based energy solver coupled with tabulated thermodynamic properties – Application to the prediction of macrosegregation in multicomponent alloys, Comput. Mater. Sci. 99 (2015) 221–231, doi:10.1016/j.commatsci.2014.12.009.

[44] Q. Chen, G. Guillemot, C.-.A. Gandin, M. Bellet, Numerical modelling of the impact of energy distribution and Marangoni surface tension on track shape in selective laser melting of ceramic material, Addit. Manuf. 21 (2018) 713–723, doi:10.1016/j.addma.2018.03.003.

[45] B. Jarvis, Keyhole gas tungsten arc welding: a new process variant, Univ. Wollongong Thesis Collect. 1954-2016. (2001). https://ro.uow.edu.au/theses/1833.

[46] E.D. Hondros, M. McLean, K.C. Mills, B.J. Keene, R.F. Brooks, A. Shirali, Marangoni effects in welding, Philos. Trans. R. Soc. Lond. Ser. Math. Phys. Eng. Sci. 356 (1998) 911–925, doi:10.1098/rsta.1998.0196.

[47] A. Traidia, Multiphysics modelling and numerical simulation of GTA weld pools, phdthesis, Ecole Polytechnique X, 2011. https://pastel.archives-ouvertes.fr/pastel-00709055 (accessed October 7, 2020).

[48] O. Hunziker, Theory of plane front and dendritic growth in multicomponent alloys, Acta Mater 49 (2001) 4191–4203, doi:10.1016/S1359-6454(01)00313-5.

[49] W. Kurz, B. Giovanola, R. Trivedi, Theory of microstructural development during rapid solidification, Acta Metall 34 (1986) 823–830, doi:10.1016/0001-6160(86)90056-8.

[50] R. Trivedi, W. Kurz, Dendritic growth, Int. Mater. Rev. 39 (1994) 49–74.

[51] G. Guillemot, C.-.A. Gandin, H. Combeau, R. Heringer, A new cellular automaton—Finite element coupling scheme for alloy solidification, Model. Simul. Mater. Sci. Eng. 12 (2004) 545.

[52] T. Carozzani, H. Digonnet, C.-.A. Gandin, 3D CAFE modeling of grain structures: application to primary dendritic and secondary eutectic solidification, Model. Simul. Mater. Sci. Eng. 20 (2011) 015010, doi:10.1088/0965-0393/20/1/015010.

[53] T. Coupez, Metric construction by length distribution tensor and edge based error for anisotropic adaptive meshing, J. Comput. Phys. 230 (2011) 2391–2405, doi:10.1016/j.jcp.2010.11.041.

[54] A. Aalilija, Ch.-A. Gandin, E. Hachem, On the analytical and numerical simulation of an oscillating drop in zero-gravity, Comput. Fluids. 197 (2020) 104362, doi:10.1016/j.compfluid.2019.104362.

[55] S. Zhang, G. Guillemot, C.-.A. Gandin, M. Bellet, A partitioned two-step solution algorithm for concurrent fluid flow and stress–strain numerical simulation in solidification processes, Comput. Methods Appl. Mech. Eng. 356 (2019) 294–324, doi:10.1016/j.cma.2019.07.006.

[56] J.W. Elmer, T.A. Palmer, W. Zhang, B. Wood, T. DebRoy, Kinetic modeling of phase transformations occurring in the HAZ of C-Mn steel welds based on direct observations, Acta Mater 51 (2003) 3333–3349, doi:10.1016/S1359-6454(03)00049-1.

[57] J. Shao, G. Yu, X. He, S. Li, R. Chen, Y. Zhao, Grain size evolution under different cooling rate in laser additive manufacturing of superalloy, Opt. Laser Technol. 119 (2019) 105662, doi:10.1016/j.optlastec.2019.105662.

[58] Thermodynamic Databases, Thermo-Calc Softw. (n.d.). https://thermocalc.com/products/databases/ (accessed July 12, 2021).

[59] MOBFE6 Technical Information, (n.d.) 8.